nature biomedical engineering

ARTICLES

https://doi.org/10.1038/s41551-021-00716-x

Check for updates

Shear-stress sensing by PIEZO1 regulates tendon stiffness in rodents and influences jumping performance in humans

Fabian S. Passini[1,2], Patrick K. Jaeger[1,2], Aiman S. Saab[3,4], Shawn Hanlon[5], Nicole A. Chittim[1,2], Matthias J. Arlt[1,2], Kim David Ferrari[3,4], Dominik Haenni[6], Sebastiano Caprara[1,2], Maja Bollhalder[1,2], Barbara Niederöst[1,2], Aron N. Horvath[1,2], Tobias Götschi[1,2], Shang Ma[7], Bettina Passini-Tall[1], Sandro F. Fucentese[1], Ulrich Blache[1,2], Unai Silván[1,2], Bruno Weber[3,4], Karin Grävare Silbernagel[5] and Jess G. Snedeker[1,2] ✉

Athletic performance relies on tendons, which enable movement by transferring forces from muscles to the skeleton. Yet, how load-bearing structures in tendons sense and adapt to physical demands is not understood. Here, by performing calcium (Ca^{2+}) imaging in mechanically loaded tendon explants from rats and in primary tendon cells from rats and humans, we show that tenocytes detect mechanical forces through the mechanosensitive ion channel PIEZO1, which senses shear stresses induced by collagen-fibre sliding. Through tenocyte-targeted loss-of-function and gain-of-function experiments in rodents, we show that reduced PIEZO1 activity decreased tendon stiffness and that elevated PIEZO1 mechanosignalling increased tendon stiffness and strength, seemingly through upregulated collagen cross-linking. We also show that humans carrying the *PIEZO1* E756del gain-of-function mutation display a 13.2% average increase in normalized jumping height, presumably due to a higher rate of force generation or to the release of a larger amount of stored elastic energy. Further understanding of the PIEZO1-mediated mechanoregulation of tendon stiffness should aid research on musculoskeletal medicine and on sports performance.

Tendons connect muscle to bone and experience some of the highest mechanical forces in the body[1]. During movements with strong body acceleration, such as sprinting and jumping, tendons store and return energy in a catapult-like manner[2] and thereby enable the muscle–tendon unit to generate more power than is possible by the muscle alone[3,4]. Interestingly, regular high-load exercising increases the mechanical properties of tendons but with little to no change in the tendon cross-sectional area[5,6]. This is confirmed by sprinters who display tendons with elevated stiffness and strength compared with endurance runners and non-active individuals[7]. Moreover, tendon diseases are conventionally treated with physical therapy that aims to restore the decreased stiffness and impaired performance by specific application of mechanical stimuli[8,9]. However, very little is known about acute cellular dynamics in response to physiological tendon loading and the underlying molecular mechanisms that regulate tendon stiffness.

Mechanotransduction is crucial to a wide variety of physiological processes, such as hearing, touch sensation, regulation of blood flow and pressure, as well as proprioception and breathing[10–15]. These events rely on molecular mechanisms that convert mechanical forces into biological signals, often using various membrane proteins. In eukaryotes, several ion channels and receptors have been identified as mechanosensors[16–24]. Among these, the mechanosensitive ion channel PIEZO1 is responsible for different mechanotransduction processes that occur in the lymphatic, cardiovascular, renal and skeletal systems[25–30]. Genetic mutations in *PIEZO1* have revealed the physiological importance of this ion channel in humans. A *PIEZO1* loss-of-function mutation leads to persistent congenital lymphoedema[25,26], while a *PIEZO1* gain-of-function mutation that is common in individuals of African descent has been associated with malaria resistance[31]. Although research on mechanically activated ion channels and receptors has made substantial progress in recent years, the mechanosensors in tendons—one of the most mechanically challenged tissues of the human body—have not been identified.

In this Article, we investigated tendon mechanotransduction by combining Ca^{2+} imaging with simultaneous mechanical loading of tendon explants and isolated primary tendon cells. The physiological role of the identified molecular mechanism was then studied with both loss-of-function and gain-of-function experiments in both mice and humans.

Results

Tenocytes sense tissue stretching through transient intracellular Ca^{2+} elevations. To investigate how tendon cells (tenocytes) detect mechanical forces, we developed a functional imaging system that enables simultaneous fluorescence microscopy and tissue stretching of tendon explants from rat tails (Fig. 1a; further details are provided in the Methods). Using this approach, we performed Ca^{2+} imaging in tissue-resident tenocytes labelled with Fluo-4. In

[1]University Hospital Balgrist, University of Zurich, Zurich, Switzerland. [2]Institute for Biomechanics, ETH Zurich, Zurich, Switzerland. [3]Institute of Pharmacology and Toxicology, University of Zurich, Zurich, Switzerland. [4]Neuroscience Center, University and ETH Zurich, Zurich, Switzerland. [5]Department of Physical Therapy, University of Delaware, Newark, DE, USA. [6]Center for Microscopy and Image Analysis, University of Zurich, Zurich, Switzerland. [7]Howard Hughes Medical Institute, Department of Neuroscience, Dorris Neuroscience Center, Scripps Research, La Jolla, CA, USA. ✉e-mail: snedeker@access.uzh.ch

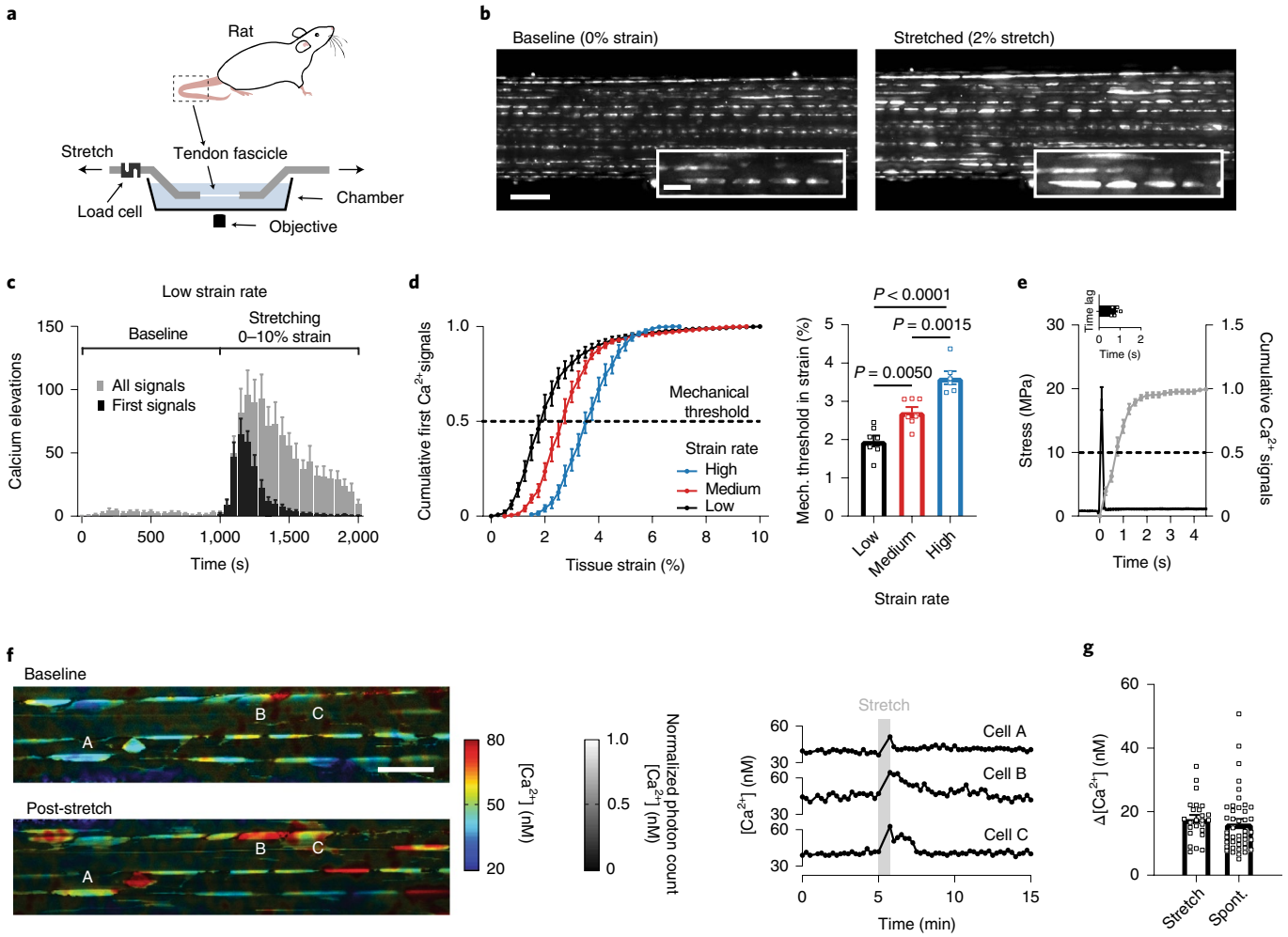

Fig. 1 | Mechanically induced Ca^{2+} elevations in tissue-resident tenocytes. a, Schematic of the set-up used for simultaneous stretching and Ca^{2+} imaging of tissue-resident tenocytes labelled with Fluo-4. **b**, Ca^{2+} images of a rat tail tendon fascicle at baseline and during the stretching protocol at a low strain rate (0.01% strain per second) showing stretch-induced Ca^{2+} signals. Scale bars, 100 µm, in the inset 20 µm. **c**, Quantification of the Ca^{2+} signals at the baseline and during the stretching protocol at a low strain rate. $n = 7$ fascicles. **d**, The cumulative sum of the first Ca^{2+} signals for three different strain rates (low, 0.01% strain per s; medium, 0.1% strain per second; and high, 1.0% strain per second) showing a right shift with increasing strain rate. The mechanical (mech.) threshold was defined at 50% of the cumulative curve and corresponds to the tissue strain at which 50% of the cells showed a first Ca^{2+} signal. Mechanical thresholds were found at (from low to high strain rate): 1.96 ± 0.35% strain ($n = 7$ fascicles), 2.72 ± 0.33% strain ($n = 7$ fascicles) and 3.62 ± 0.38% strain ($n = 6$ fascicles). Statistical analysis was performed using one-way ANOVA with testing for multiple comparisons (Tukey test). **e**, Quantification of the time lag between mechanical stimulus and Ca^{2+} elevation. $n = 5$ fascicles. **f**, FLIM-acquired images of OGB-1-labelled tenocytes in a rat tail tendon fascicle showing the $[Ca^{2+}]$ landscapes at the baseline and after stretch. Scale bar, 50 µm. Corresponding time traces of $[Ca^{2+}]$ for three cells (indicated by the letters in the images). **g**, Quantification of the increases in $[Ca^{2+}]$, represented as $\Delta[Ca^{2+}]$, between the baseline and the active state for stretch-induced Ca^{2+} signals ($n = 25$ cells from 6 fascicles) and spontaneous (spont.) Ca^{2+} signals ($n = 43$ cells from 13 fascicles). Replicates are biological. Data are mean ± s.e.m.

the unstretched condition, we detected sparse spontaneous Ca^{2+} signals; however, after stretching from 0–10% strain, we observed a tissue-wide Ca^{2+} response (Fig. 1b and Supplementary Videos 1 and 2), with Ca^{2+} signals lasting 28.2 ± 16.5 s (mean ± s.d.). By testing different strain rates, we noticed distinct Ca^{2+} dynamics. At a low strain rate, each tenocyte exhibited multiple Ca^{2+} signals, whereas, at a high strain rate, they displayed only a single Ca^{2+} response after tendon stretching (Fig. 1c and Supplementary Fig. 1). Furthermore, with increasing strain rate, higher tissue stretch was required to elicit a Ca^{2+} response in 50% of the cells (Fig. 1d). This strain rate dependency can be partially explained by a time lag between stimulus and Ca^{2+} signal of 0.77 ± 0.18 s (Fig. 1e). We attributed the remaining differences to the inherent viscoelastic properties of the tissue (Supplementary Fig. 1e) and to potential cell-cell communication processes occurring predominately at a low strain rate (Supplementary Video 3). Compared with identified limits of tissue damage[32] and in vivo measurements of tendon tissue strains[33], the identified mechanical thresholds were found to reside near the upper limits of the physiological range. This suggests that the mechanical thresholds probably represent a 'limit switch' for mechanical-load-induced tissue deformation that triggers tissue adaptation.

The stretch-induced Ca^{2+} response was confirmed using two-photon fluorescence lifetime imaging (FLIM), using which we also determined the absolute Ca^{2+} concentrations in tissue-resident tenocytes (Supplementary Fig. 2) after OGB-1 (Oregon Green

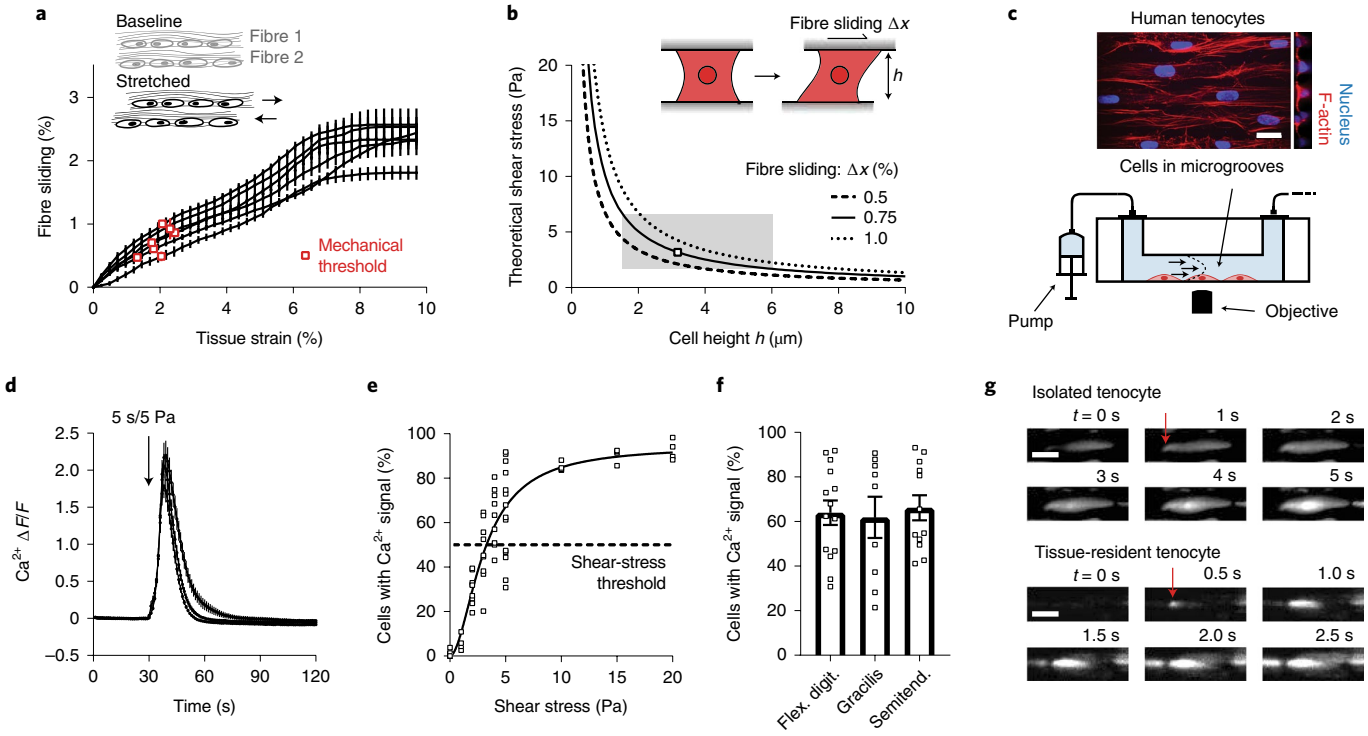

Fig. 2 | Shear stress as a key stimulus driving Ca^{2+} signals in isolated tenocytes. a, Fibre sliding quantified on the basis of images of rat fascicles stretched at a low strain rate (Fig. 1c,d) by measuring the relative displacements between adjacent fibres. Data are mean ± s.e.m. for each of the $n = 7$ fascicles. The corresponding mechanical thresholds are indicated by red squares and were defined as the tissue strain at which 50% of the cells showed the first Ca^{2+} signal (Fig. 1d). **b**, Theoretical shear stresses that act on tenocytes due to fibre sliding. Shear stresses were calculated for three different levels of fibre sliding (0.5%, 0.75% and 1.0%). The predicted mechanosensitive zone of tenocytes is shown as a grey box. **c**, Schematic of the flow chamber used for Ca^{2+} imaging of isolated tenocytes during shear-stress stimulations. The flow chamber included aligned microchannels to promote a native cell morphology. Scale bar, 20 μm. **d**, Shear stress (5 Pa for 5 s, onset indicated by arrow) induces Ca^{2+} signals in human tenocytes. $\Delta F/F = (F(t) - F_0)/F_0$, where $F(t)$ is the fluorescence signal at a given time (t) and F_0 is the baseline fluorescence signal. $n = 12$ chambers, cells from flexor digitorum tendons, $n = 3$ human donors. **e**, Tenocytes display an increased response rate with increasing shear stress. For each condition, $n \geq 4$ chambers, cells from flexor digitorum tendons, $n = 2$ or 3 human donors. A nonlinear fit with hill slope ($y = \frac{94.42\ x^h}{3.08^h + x^h}$; $h = 1.854$; $R^2 = 0.862$) was performed to identify the shear-stress threshold, which was defined at 50% of the fit and corresponds to the shear stress at which 50% of the cells show a Ca^{2+} signal. **f**, There was no difference in the Ca^{2+} response to shear stress (5 Pa for 5 s) in tenocytes from different anatomical locations. For each condition, $n \geq 9$ chambers, cells from 2 or 3 human donors. Statistical analysis was performed using one-way ANOVA with testing for multiple comparisons (Tukey test). Flex. digit., flexor digitorum; semitend., semitendinosus. **g**, Representative images of Ca^{2+} signals originating at the cell periphery (indicated by arrows) observed in hundreds of cells, both in vitro (shear stress, cells from a human flexor digitorum tendon) and in situ (tissue stretch, cells in a rat tail tendon fascicle). Scale bars, 20 μm. Replicates are biological. Data are mean ± s.e.m.

BAPTA-1) loading[34]. At rest, Ca^{2+} levels averaged 43 ± 4 nM (mean ± s.d.); however, after tissue stretching, Ca^{2+} levels increased by 18 ± 6 nM reaching on average 61 ± 8 nM (Fig. 1f). Similar Ca^{2+} elevations of 16 ± 9 nM were detected in spontaneous signals, indicating that the stretch-induced Ca^{2+} responses were in the physiological range (Fig. 1g). Taken together, we observed a mechanosensitive Ca^{2+} response in tenocytes that depends both on the magnitude and rate of the tissue stretch.

Shear stress triggers Ca^{2+} signals in isolated tenocytes. During tissue stretching, collagen fibres—the load-bearing elements of the extracellular matrix—slide past each other[35]. Tenocytes reside between these fibres and are therefore exposed to mechanical shear. As fibre sliding is the predominant mechanism enabling the extension of tendon fascicles[35], we wondered whether shear stress could be the primary mechanical stimulus for tenocytes. We therefore quantified the fibre sliding by tracking cells from image sequences obtained at low strain rates and by comparing interfibre displacements (Fig. 2a) and, using a physical model, we calculated the resulting shear stress, which ranged between 2 Pa and 6 Pa depending on the cell height (Fig. 2b). Our analysis suggests that shear-stress levels may vary across cellular domains of tenocytes, probably being highest around narrow protrusions and lowest around the cell body. To test our prediction, we developed a microfluidics flow chamber that enables simultaneous Ca^{2+} imaging and shear-stress stimulation of isolated primary tenocytes stained with Fluo-4 (Fig. 2c and Supplementary Fig. 3; further details are provided in the Methods). Exposing tenocytes to a shear stress of 5 Pa, which occurs during tissue stretching, triggered a prominent Ca^{2+} response (Fig. 2d and Supplementary Video 4). The magnitude of shear-stress stimulus determines the percentage of responsive cells (Fig. 2e) as well as the amplitude and duration of the Ca^{2+} response (Supplementary Fig. 4). A Ca^{2+} response in about 50% of tenocytes is induced by a shear stress of 3.3 Pa, which falls well within the range of the calculated shear stress that occurs during tissue stretching (Fig. 2b). Together, this confirms the role of shear stress as a key mechanical stimulus for tenocytes, which show similar responsiveness across anatomical regions (Fig. 2f).

We noticed that Ca^{2+} signals typically start at the cell periphery both in isolated and in tissue-resident tenocytes (Fig. 2g). This

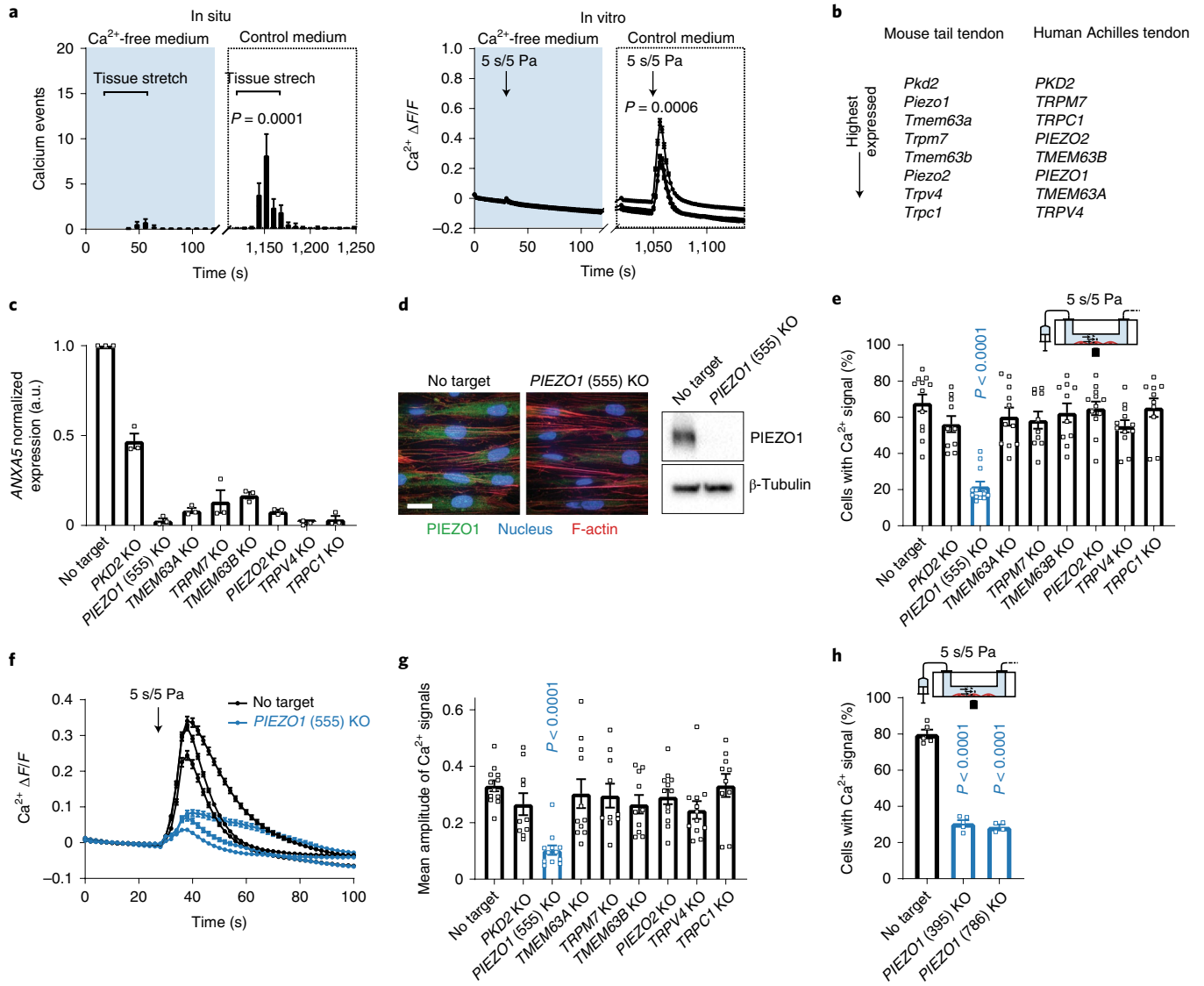

Fig. 3 | PIEZO1-mediated shear-stress response in human tenocytes. a, Mechanically induced Ca^{2+} signals are nearly absent in Ca^{2+}-free medium (containing 2 mM EGTA and 2 mM $MgCl_2$ instead of $CaCl_2$) but are restored in control medium, both in situ (one cycle stretch to 2.7% strain at 0.1% strain per s; $n = 7$ fascicles from rat tails) and in vitro (shear-stress stimulation; $n = 12$ chambers, cells from semitendinosus tendons of 3 human donors). Statistical analysis was performed using paired Student's *t*-tests. **b**, The highest expressed candidate genes associated with mechanosensitive ion channel characteristics selected from RNA-sequencing experiments with mouse tail tendons[37] and human Achilles tendons[38]. **c**, CRISPR–Cas9-mediated knockout efficiency of candidate genes. Normalization to gene expression in no-target control cells was performed using the $2^{-\Delta\Delta C_t}$ method (cells from $n = 3$ human donors). 555 in brackets indicates the site in *PIEZO1* targeted by the CRISPR–Cas9. There was a significant reduction ($P < 0.0001$) for all candidates compared with the no-target control. **d**, Immunofluorescence images and western blot analysis (the full scan is provided in Supplementary Fig. 5) showing efficient *PIEZO1* knockout in human *PIEZO1*-knockout tenocytes compared with the no-target control tenocytes. Scale bar, 20 µm. **e**, The Ca^{2+} response of the candidate knockouts to a shear-stress stimulus of 5 Pa for 5 s. PIEZO1-depleted cells show a reduced percentage of responsive cells. For each candidate, $n \geq 10$ chambers were tested with cells from $n = 3$ human donors (semitendinosus tendons). **f**, The corresponding Ca^{2+} signals over time for *PIEZO1*-knockout tenocytes and no-target control tenocytes (averaged over all single segmented cells for the $n = 3$ human donors). **g**, The corresponding mean amplitude of the Ca^{2+} signals observed in the candidate knockouts. PIEZO1-depleted cells show a reduced amplitude of the Ca^{2+} signals. **h**, Two additional *PIEZO1* knockouts generated using different CRISPR-guided RNAs (395 and 786 indicate the two different sites targeted by CRISPR–Cas9) confirm the reduced shear-stress response. $n \geq 4$ chambers, cells from a human semitendinosus tendon. Unless indicated otherwise, statistical analysis was performed using one-way ANOVA with testing for multiple comparisons (Dunnett test). Replicates are biological. Data are mean ± s.e.m.

is consistent with our physical model that predicts that narrow regions (that is, protrusions) experience the highest levels of shear stress.

PIEZO1 is required for the shear-stress-induced response in tenocytes. As mechanotransduction relies on membrane proteins that convert mechanical stimuli into a biological signal[36], we wondered whether shear stress in tenocytes activates mechanosensitive membrane channels mediating the Ca^{2+} influx. To test this, we performed mechanical stimulation in Ca^{2+}-free medium and observed no overt Ca^{2+} response in tissue-resident and isolated tenocytes (Fig. 3a). However, reperfusion with control medium containing Ca^{2+} restored the stimulus-evoked responses (Fig. 3a), suggesting a channel-mediated mechanism.

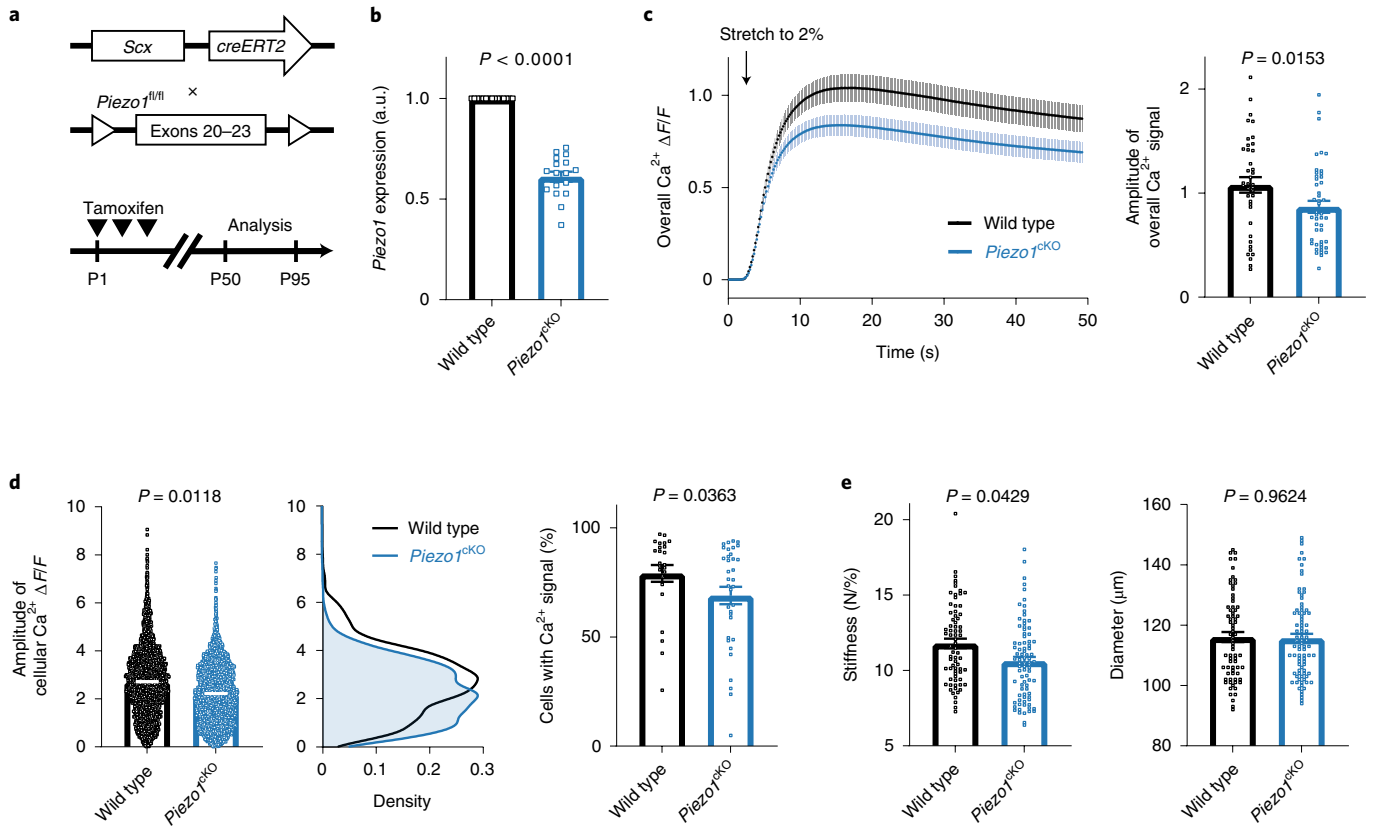

Fig. 4 | Decreased stretch-induced Ca^{2+} response and stiffness in fascicles from tenocyte-targeted *Piezo1*-knockout mice. a, Generation of *Scx-creERT2*; *Piezo1*$^{fl/fl}$ mice expressing *creERT2* under the *Scx* promoter. Tamoxifen injections were performed at P1–P3 and the analysis was carried out between P50 and P95. **b**, Reduced *Piezo1* expression in tail tendon fascicles from *Piezo1*^{cKO} mice (*Scx-creERT2*; *Piezo1*$^{fl/fl}$, $n = 17$ mice) compared with their wild-type littermates (*Piezo1*$^{fl/fl}$, $n = 15$ mice). *Anxa5* was used as the reference gene. Statistical analysis was performed using unpaired Student's *t*-tests. **c**, The overall stretch-induced Ca^{2+} response is reduced in fascicles from 7- to 11-week-old *Piezo1*^{cKO} mice ($n = 9$ mice) compared with wild-type littermate controls ($n = 6$ mice). $n = 6$ fascicles were tested per mouse. **d**, Corresponding single-cell analysis shows that tenocytes in fascicles from *Piezo1*^{cKO} mice exhibit a reduced amplitude of the stretch-induced Ca^{2+} signals and a reduced percentage of responsive cells. **e**, Ramp-to-failure tests show a decreased stiffness (measured in the force–strain curve; force in N, strain in %) of fascicles from 10- to 13-week-old *Piezo1*^{cKO} mice ($n = 14$ mice) compared with wild-type littermate controls ($n = 12$ mice). $n = 6$ fascicles tested per mouse. Unless indicated otherwise, statistical analysis was performed using linear mixed-effects models (mouse ID was used as a random effect and litter as a fixed effect). Replicates are biological. Data are mean ± s.e.m.

To identify the responsible ion channel, we focused on candidates associated with mechanosensitive cation channel characteristics that are highly expressed in both mouse tail tendons[37] and human Achilles tendons[38] (Fig. 3b). Using CRISPR–Cas9 genome editing, we generated efficient knockdowns of the selected genes in human primary tenocytes and tested their mechanosensitive response (Fig. 3c,d). From all examined knockdowns, only cells depleted of PIEZO1, which is known to be a shear sensor[12,16,39], showed a significant reduction in the shear-stress response (Fig. 3e–g). This was further corroborated by analysing additional CRISPR-guided RNAs targeting different regions of *PIEZO1* (Fig. 3h), thereby also precluding the contribution of potential off-target effects. Moreover, we obtained similar results with CRISPR–Cas9-mediated *Piezo1* knockdowns in rat tenocytes isolated from tail tendon fascicles (Supplementary Fig. 6a–e). This suggests that PIEZO1, which is an abundantly expressed ion channel in tendon tissues (Supplementary Fig. 6f), is the crucial shear-stress sensor in tenocytes.

Next, to further assess whether PIEZO1 also mediates mechanosensing in tissue-resident tenocytes, we generated tenocyte-targeted, conditional *Piezo1* knockout mice (*Piezo1*^{cKO}) by crossing mice expressing the tamoxifen-sensitive Cre-recombinase CreERT2 under the *Scleraxis* promoter (*Scx-creERT2*)[40] with mice carrying the loxP-flanked *Piezo1* alleles. *Scx-creERT2*; *Piezo1*$^{fl/fl}$ pups were injected at postnatal days P1–P3 with tamoxifen (Fig. 4a), which led to a 40% reduction in *Piezo1* mRNA expression in tail tendon fascicles from 7–13-week-old *Piezo1*^{cKO} mice compared with their *Piezo1*$^{fl/fl}$ littermate controls (Fig. 4b). Even with only a partial reduction in *Piezo1* expression, fascicles from *Piezo1*^{cKO} mice and their resident tenocytes showed a reduced stretch-induced Ca^{2+} response compared with littermate controls (Fig. 4c,d). This loss-of-function experiment provides further support that PIEZO1 is a tendon mechanosensor.

PIEZO1 activity regulates the biomechanical properties of tendons. To investigate the role of PIEZO1 in tendons, we performed in vitro and in vivo experiments. First, using ramp-to-failure tests, we characterized the biomechanical properties of the tail tendon fascicles from *Piezo1*^{cKO} mice and littermate controls. We found on average a 10% reduction in stiffness in fascicles from *Piezo1*^{cKO} mice (Fig. 4e). This effect was not caused by differences in the diameter of the fascicles (Fig. 4e), suggesting that PIEZO1 regulates the tendon tissue stiffness.

To further examine this PIEZO1 function, we wondered whether recurrent PIEZO1 activation in tenocytes is sufficient to adjust tissue stiffness in tendons. In cultured tendon fascicles, we first confirmed that pharmacological activation of PIEZO1 by the specific agonist

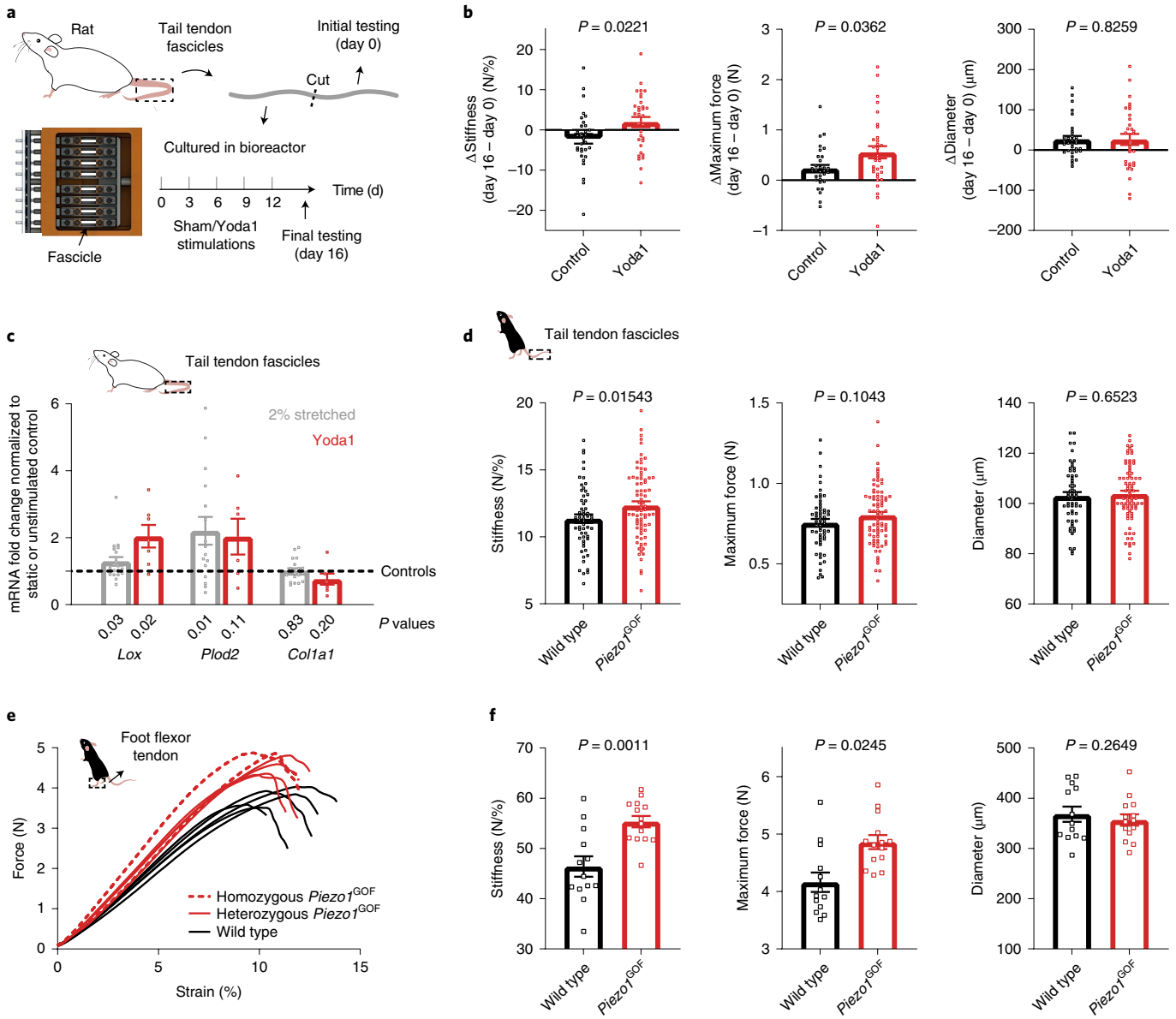

Fig. 5 | Stiffness and strength regulation of murine tendons by PIEZO1. a, Schematic of our in vitro experiment in which tendon explants were subjected to recurrent sham (control) or 5 μM Yoda1 stimulations. To investigate the changes over time, each tendon fascicle was cut in two—the first half was tested at day 0 and the second half was tested after the stimulation paradigm at day 16. **b**, Comparison of the ramp-to-failure tests between day 0 and day 16 shows higher Δstiffness (control, −2.22 N/%; Yoda1, +1.94 N/%) and Δstrength (control, +0.23 N; Yoda1, +0.55 N) after Yoda1-treatment, with no difference in Δdiameter. Strength was defined as the maximum force in the force–strain curve. $n = 32$ fascicles, $n = 4$ rats. Statistical analysis was performed using Mann–Whitney *U*-tests. **c**, mRNA expression of genes encoding collagen cross-linking enzymes (*Lox* and *Plod2*) and type-I collagen (*Col1a1*) in tendon explants 48 h after four-times stretching to 2% (normalized to static control using the $2^{-\Delta\Delta C_t}$ method; $n = 20$ samples, one sample corresponds to 4 pooled fascicles, $n = 7$ rats) or 5 μM Yoda1 stimulation (normalized to sham control using the $2^{-\Delta\Delta C_t}$ method; $n = 8$ samples, one sample corresponds to 5 pooled fascicles, $n = 4$ rats). Statistical analysis was performed using one-sample *t*-tests. **d**, Positional tendons: ramp-to-failure tests with tail tendon fascicles show an increased stiffness but unaffected diameter in *Piezo1*^{GOF} mice ($n = 13$ mice, 10 heterozygous and 3 homozygous, $n = 6$ fascicles tested per mouse) compared with wild-type littermate controls ($n = 9$ mice, $n = 6$ fascicles tested per mouse) from $n = 6$ litters in total. **e**,**f**, Load-bearing tendons: ramp-to-failure curves of plantaris tendons from littermates demonstrate a tendon phenotype in *Piezo1*^{GOF} mice (**e**) with increased stiffness and strength but unaffected diameter (**f**). $n = 8$ *Piezo1*^{GOF} mice (6 heterozygous and 2 homozygous) and $n = 7$ wild-type littermate controls were analysed from $n = 3$ litters in total. Unless indicated otherwise, statistical analysis was performed using linear mixed-effects models with Bonferroni–Holm correction (mouse ID was used as a random effect and litter as a fixed effect). Replicates are biological. Data are mean ± s.e.m.

Yoda1 (ref. [41]) triggers a robust Ca^{2+} response in tendon-resident tenocytes (Supplementary Fig. 6g and Supplementary Video 5). Next, we maintained tendon fascicles from rat tails in our custom bioreactor[42] with minimal loading to preserve tissue integrity[42] and stimulated tenocytes with 5 μM Yoda1 for 30 min every 3 d for 2 weeks (mimicking exercise; Fig. 5a). To characterize changes in biomechanical properties over time, we cut each tendon fascicle in two, tested the first half at day 0 and the second half after the stimulation paradigm at day 16 (Fig. 5a). By comparing the ramp-to-failure tests of the two time points, we noticed that stiffness and strength

were significantly higher in the Yoda1-stimulated fascicles relative to the control fascicles (Fig. 5b). However, fascicle diameter was not affected (Fig. 5b). Yoda1-stimulated fascicles showed a 4.1% average stiffness increase in the 16 d of culture. Interestingly, in humans, a 14-week exercise intervention (four-times a week) with high-magnitude tendon strain induced a 36% increase in Achilles tendon stiffness[5], corresponding to a 5.9% increase in 16 d. Thus, our data suggest that the tissue stiffness adaptation found in vitro is comparable to in vivo exercise effects.

Moreover, at the gene expression level, Yoda1 stimulation of the fascicles induces an upregulation of the collagen cross-linking enzyme LOX but not of type-I collagen (Fig. 5c). A similar gene expression profile was also observed after stretching four times to 2% (Fig. 5c), which corresponds to the mechanical threshold identified in our Ca^{2+}-imaging experiments (Fig. 1d). This shows a notable degree of overlap between pharmacological PIEZO1 stimulation and mechanical stimulation of tendon fascicles.

To verify whether increased PIEZO1-mediated mechanosignalling regulates tendon stiffness also in vivo, we analysed tendons from mice carrying a *Piezo1* gain-of-function (*Piezo1*^{GOF}) mutation equivalent to a human *PIEZO1* gain-of-function mutation (R2456H)[31]. These mice express an overactive PIEZO1 that elicits stronger Ca^{2+} signals after channel activation due to a longer inactivation time[31]. Ramp-to-failure experiments with tail tendon fascicles showed on average a 9% increase in stiffness (Fig. 5d), which is consistent with the role of PIEZO1 in regulating the mechanical properties observed in vitro and in *Piezo1*^{cKO} mice. We next wondered whether tendons that are critical for power performance (that is, load-bearing tendons) exhibit a more-pronounced phenotype as they are subjected to higher mechanical loads. We therefore tested the plantaris tendons (foot flexor tendon), and found an average increase in stiffness and strength of 19% and 17%, respectively, in *Piezo1*^{GOF} mice compared with wild-type littermates, while the macroscale tendon morphology remained unchanged (Fig. 5e,f). These biomechanical differences were particularly prominent at high tendon strains and can probably be attributed to a tenocyte-specific effect, but we cannot rule out other contributing factors as these mice are constitutive *Piezo1*^{GOF} mice (gain-of-function mutation in all tissues). However, given that PIEZO1 activation in tissue-resident tenocytes regulates the stiffness of tendon explants (Fig. 5b) and tenocyte-targeted *Piezo1*^{cKO} mice show tail tendon fascicles with reduced stiffness (Fig. 4e), our data indicate that the tendon phenotypes in *Piezo1*^{GOF} mice are primarily caused by a tenocyte-specific effect. Interestingly, load-bearing tendons of *Piezo1*^{GOF} mice revealed tissue adaptations that are very similar to differences found in tendons of sprinters compared with endurance runners and non-active individuals[7].

PIEZO1 regulates tissue stiffness by adjusting collagen cross-linking. To investigate the mechanisms that are involved in regulating the tendon mechanical properties in *Piezo1*^{GOF} mice, we first analysed the collagen fibrils—the load-bearing microstructures of tendons[35]. However, tendons of *Piezo1*^{GOF} mice revealed no overt differences in fibril size distribution compared to their wild-type littermates (Fig. 6a–c). Thus, elevated mechanosignalling by PIEZO1 regulates tendon stiffness and strength without inducing hypertrophic collagen production. Similarly, exercise-induced increases in tendon mechanical properties were not associated with changes in collagen fibril morphology[43]. This probably indicates that the regulation of tendon stiffness and strength in response to mechanosignalling may be induced by a denser collagen cross-linking[44]. To address this, we performed differential scanning calorimetry measurements and assessed the tissue thermal stability, which depends on the cross-link density[45]. Tendons from *Piezo1*^{GOF} mice showed an elevated transition enthalpy, demonstrating an increased thermal stability compared with their wild-type littermates (Fig. 6d). Thus, this finding indicates an elevated cross-link density in tendons from *Piezo1*^{GOF} mice. Moreover, using two-photon microscopy we observed an increased autofluorescence signal associated with the pyridinoline-cross-links relative to the second-harmonic-generation signal associated with the collagen matrix[46] (Fig. 6e). Although little is known about the specific contribution of individual cross-links to the mechanical properties of tendons, our data suggest a denser pyridinoline-cross-link network in the tendons of *Piezo1*^{GOF} mice.

PIEZO1 activity influences jumping performance in humans. Strong, stiff tendons are critical for high physical performance[3] and we wondered whether our observed PIEZO1-mediated adaptations in tendon stiffness and strength could be relevant for human athletic performance. In fact, about one out of three individuals of African descent carries a *PIEZO1*^{GOF} mutation known as E756del, which has been associated with malaria resistance and represents the most abundant *PIEZO1*^{GOF} mutation identified to date—it is particularly common in West African populations[31]. Whether the E756del allele is overrepresented in elite athletes is unknown. Although self-reported race serves as a poor proxy for genetic ancestry[47,48], athletes hailing from countries with high E756del prevalence disproportionally populate the ranks of elite sprinters and jumpers[49–51]. But could human E756del carriers also present tendon adaptations that associate with athletic performance? We addressed this question in a double-blind study in which we investigated Achilles tendons of 65 healthy African Americans and assessed their jumping performance.

Genotyping identified 20 heterozygous and 2 homozygous E756del carriers, and 43 non-carrier controls (Fig. 7a). We observed comparable demographics and whole-body morphometry between E756del carriers and non-carriers, with no differences in age, height, weight, physical activity or sports participation (Fig. 7b and Supplementary Fig. 7). Ultrasound-based assessment of the Achilles tendon morphology showed no significant differences in tendon cross-sectional area and the length between E756del carriers and non-carriers (Fig. 7c,d), which is consistent with the unchanged tendon morphology observed in *Piezo1*^{GOF} mice (Fig. 5f). As the tendon phenotype in *Piezo1*^{GOF} mice was prominent at high degrees of tendon loading, we speculated that human E756del carriers may show athletic differences in exercises that evoke high tendon loading. We therefore measured the participant's maximal jumping performance in two related jumps, namely, a countermovement jump (CMJ) and a drop countermovement jump (DCMJ) (Fig. 7e). The latter differs solely by an initial drop from a height of 20 cm, which leads to greater mechanical loads in the Achilles tendon[52,53]. Importantly, as we anticipated a high variability in performance between participants, we chose a study design that would enable an intraindividual comparison using the two jumping modalities to evoke different levels of tendon loading (CMJ < DCMJ) to properly address differences in tendon-loading exercises between groups. Indeed, the overall performance varied highly between individuals (Fig. 7f). However, the intraindividual comparison revealed that E756del carriers performed significantly better in DCMJ, which evokes higher tendon loading, compared with CMJ, whereas non-carrier controls performed similarly in both jumps (Fig. 7f). By accounting for the interindividual jumping variability with the normalization of individual DCMJ to CMJ, we found an average performance of 110.9% in E756del carriers that significantly exceeded the average 97.7% reached by non-carriers (Fig. 7g). Thus, E756del carriers showed a net 13.2% average increase in normalized jumping performance compared with non-carriers, presumably due to a higher rate of force development (body acceleration) or a greater capacity of tendons to store and return elastic energy. Indeed, when converting the jump height into potential energy (that is mass × gravitational acceleration × jump height), we found that E756del carriers effectively stored and returned the drop energy (+8.1 J on average), whereas

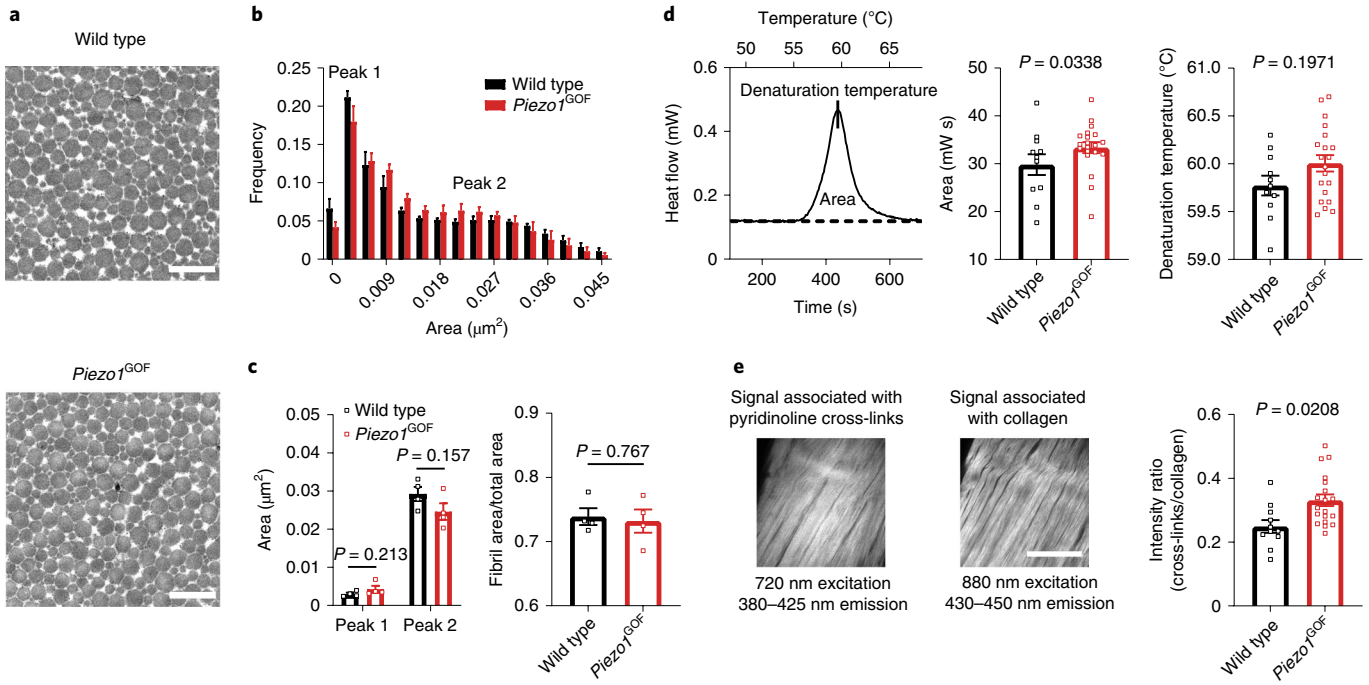

Fig. 6 | Unchanged collagen fibrils but increased cross-link-associated thermal stability and autofluorescence in load-bearing tendons from *Piezo1*^{GOF} mice. a, Transmission electron microscopy images showing the collagen fibrils in plantaris tendons from a *Piezo1*^{GOF} mouse and a wild-type littermate. Scale bars, 500 nm. **b**, Quantification of the collagen fibril area from transmission electron microscopy images of plantaris tendons shows a similar frequency distribution between *Piezo1*^{GOF} mice and wild-type littermates. An average of around 23,600 collagen fibrils were analysed per tendon. $n = 1$ tendon per mouse, $n = 4$ mice per genotype. **c**, No differences were observed in the two local peaks determined with a fit of the frequency distribution. $n = 4$ mice per genotype. Statistical analysis was performed using multiple *t*-tests. The tissue compactness, measured as the ratio between fibril area and total area, was also similar between plantaris tendons from *Piezo1*^{GOF} mice and wild-type littermates. $n = 4$ mice per genotype. Statistical analysis was performed using unpaired Student's *t*-tests. **d**, Differential scanning calorimetry measurements with Achilles tendons demonstrate an increased transition enthalpy, corresponding to the area between the denaturation curve and the baseline (shown as a dashed line) in *Piezo1*^{GOF} mice ($n = 10$ mice, 8 heterozygous and 2 homozygous) compared with wild-type littermate controls ($n = 6$ mice). **e**, Two-photon imaging of Achilles tendons was used to assess the autofluorescence associated with the collagen cross-links pyridinoline, and the second-harmonic-generation signal associated with the collagen matrix[46]. $n = 11$ *Piezo1*^{GOF} mice (8 heterozygous and 3 homozygous) and $n = 7$ wild-type littermate mice. Scale bar, 100 μm. Unless indicated otherwise, statistical analysis was performed using linear mixed-effects models (mouse ID was used as a random effect and litter as a fixed effect). Replicates are biological. Data are mean ± s.e.m.

the non-carriers did not (−1.7 J on average; Fig. 7h). Accounting for the energy return of E756del carriers against the energy dissipation of non-carriers, E756del carriers showed on average a significantly increased net energy return of 9.8 J. Thus, the E756del mutation probably influences sports performances that rely on the power output generated with high tendon loading, such as sprinting and jumping.

Discussion

In tendon mechanotransduction, it has been hypothesized that mechanical forces are converted into biological signals by mechanically activated membrane proteins[54,55]. Isolated tenocytes are sensitive to pipette indentation[56] and show increased frequency of spontaneous Ca^{2+} signals after a mechanical stimulation[57]. However, evidence of acute responses to physiologically relevant mechanical stimuli and the underlying molecular sensing mechanisms is lacking.

We developed a microscope-compatible functional imaging setup to enable the direct observation of tenocytes during tissue stretching and harnessed it to characterize tendon mechanotransduction by Ca^{2+} imaging. After tissue stretching, we observed that tenocytes exhibit simultaneous Ca^{2+} signals occurring tissue-wide, whereas, in the unstretched condition, they show only a few sparce spontaneous Ca^{2+} signals. Thus, the tissue-wide spatiotemporal Ca^{2+} profile differs clearly during a mechanical stimulus, probably triggering a mechanobiological response of the tissue. Furthermore, we noticed that, at a low strain rate, less stretch was required to elicit the response in tenocytes. This phenomenon might explain why physical rehabilitation strategies based on slowly performed resistance training show improved outcomes when treating tendinopathies[58,59]. Our data suggest that these improvements might arise from an optimal compromise between maximizing cellular stimulation while minimizing tissue strains and loads.

Moreover, we identified shear stress as a key mechanical stimulus by determining the shear-stress levels that occur during tissue stretching, applying them to isolated primary rat and human tendon cells and finding tight activation limits in vitro and in situ. By combining functional Ca^{2+} imaging with CRISPR–Cas9 screening and in vivo tenocyte-targeted loss of function, we found that PIEZO1 is a tendon mechanosensor that is crucial for shear-stress-induced Ca^{2+} signals.

To investigate the role of this ion channel in tendons, we analysed the effect of reduced as well as elevated PIEZO1 mechanosignalling in tendons of rodents. Tenocyte-targeted *Piezo1*^{cKO} mice showed tail tendon fascicles with reduced stiffness. By contrast, in vitro pharmacological PIEZO1 stimulation and in vivo PIEZO1 overactivity increased tendon stiffness and strength. Surprisingly, these changes do not seem to result from a hypertrophic tissue response; instead,

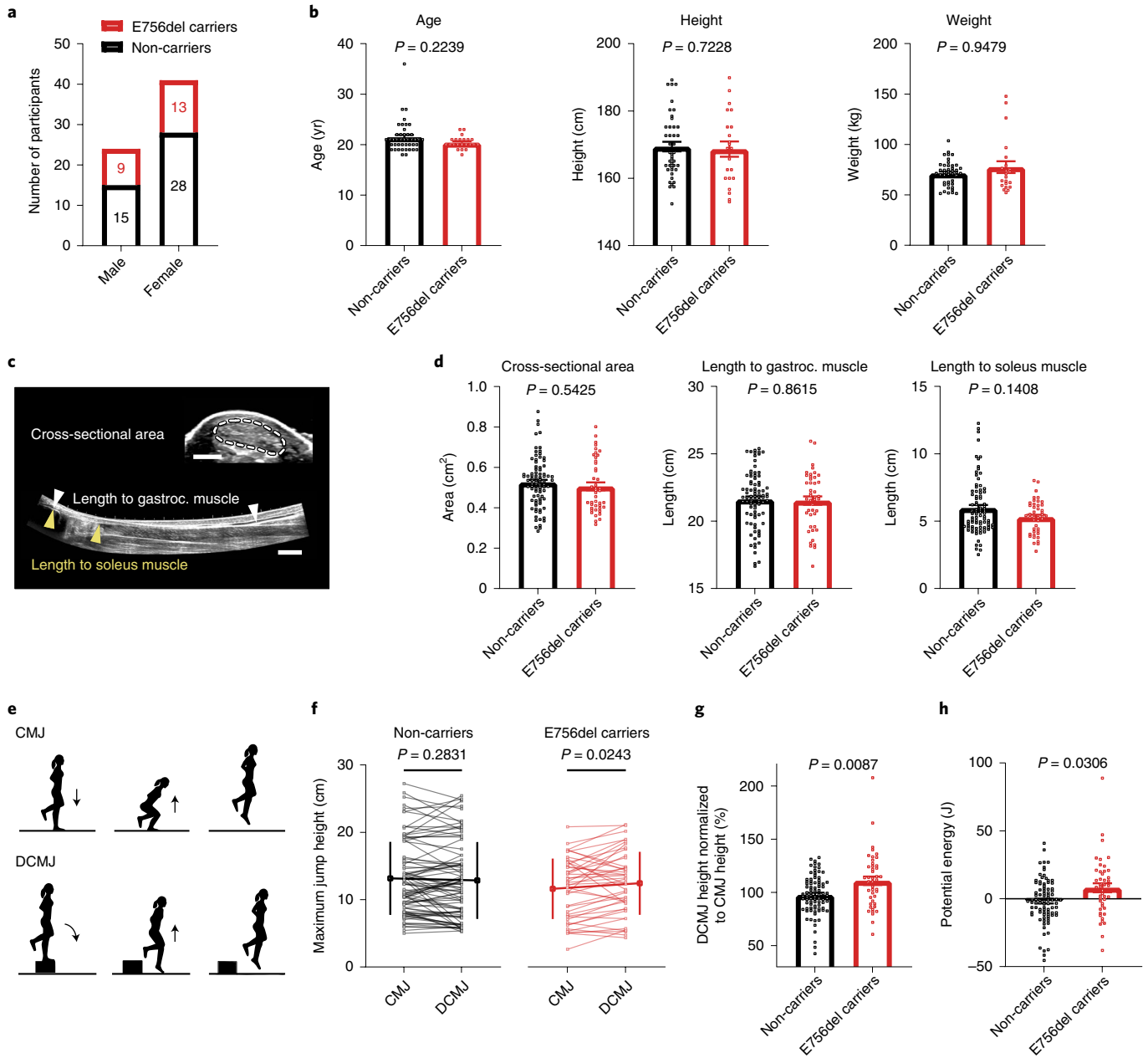

Fig. 7 | Human jumping performance is influenced by *PIEZO1*^{GOF} E756 mutation with no effect on Achilles tendon morphology. a,**b**, Genotyping identified $n = 22$ E756del carriers and $n = 43$ non-carriers in the 65 African-American participants (**a**) with no differences in age, height and weight between the two groups (**b**). Statistical analysis was performed using Mann–Whitney *U*-tests. **c**, Ultrasound imaging was used to assess the cross-sectional area (scale bar, 0.5 cm) and the length (scale bar, 2 cm) of the Achilles tendon. **d**, The cross-sectional area and the length to the gastrocnemius (gastroc.) muscle and to the soleus muscle of the Achilles tendon were unaffected by the E756del mutation. **e**, Schematic of single-leg CMJ and single-leg DCMJ, which was used to assess jumping performance. CMJ and DCMJ differ solely by the initial drop (from 20 cm) in DCMJ, which leads to greater Achilles tendon loading. For each leg and jump, the average of three trials was used for analysis. **f**, The average jumping heights between non-carriers and E756del carriers were similar (CMJ, 13.1 ± 5.4 versus 11.6 ± 4.4 cm ($P = 0.25$); and DCMJ, 12.8 ± 5.7 versus 12.4 ± 4.6 cm ($P = 0.77$)). Data are mean ± s.d. (represented on the sides). However, intraindividual analysis within non-carriers revealed a similar performance in both jumps ($P = 0.28$), whereas, within E756del carriers, the performance was significantly better in DCMJ compared with CMJ ($P = 0.02$, paired analysis). Performances corresponding to the same leg are connected with a line. **g**, Normalization of the DCMJ height to the CMJ height to isolate the effect of greater tendon loading shows a significant increase in normalized jumping height in E756del carriers compared with non-carriers. **h**, Conversion of jump height difference (between DCMJ and CMJ) into potential energy demonstrates that E756del carriers more effectively transformed the drop energy into jump height. Statistical analysis was performed using linear mixed-effects models unless indicated otherwise (individual ID was used as a random effect and leg as a fixed effect). Both legs of $n = 22$ E756del carriers and $n = 43$ non-carriers were analysed. Replicates are biological. Unless indicated otherwise, data are mean ± s.e.m.

they are probably caused by collagen cross-linking, as we found elevated thermal stability and autofluorescence associated with pyridinoline-cross-links in tendons from *Piezo1*^{GOF} mice. This is consistent with the gene expression profile triggered by both pharmacological PIEZO1 activation and mechanical stretching that revealed an upregulation of collagen cross-linking enzymes but not

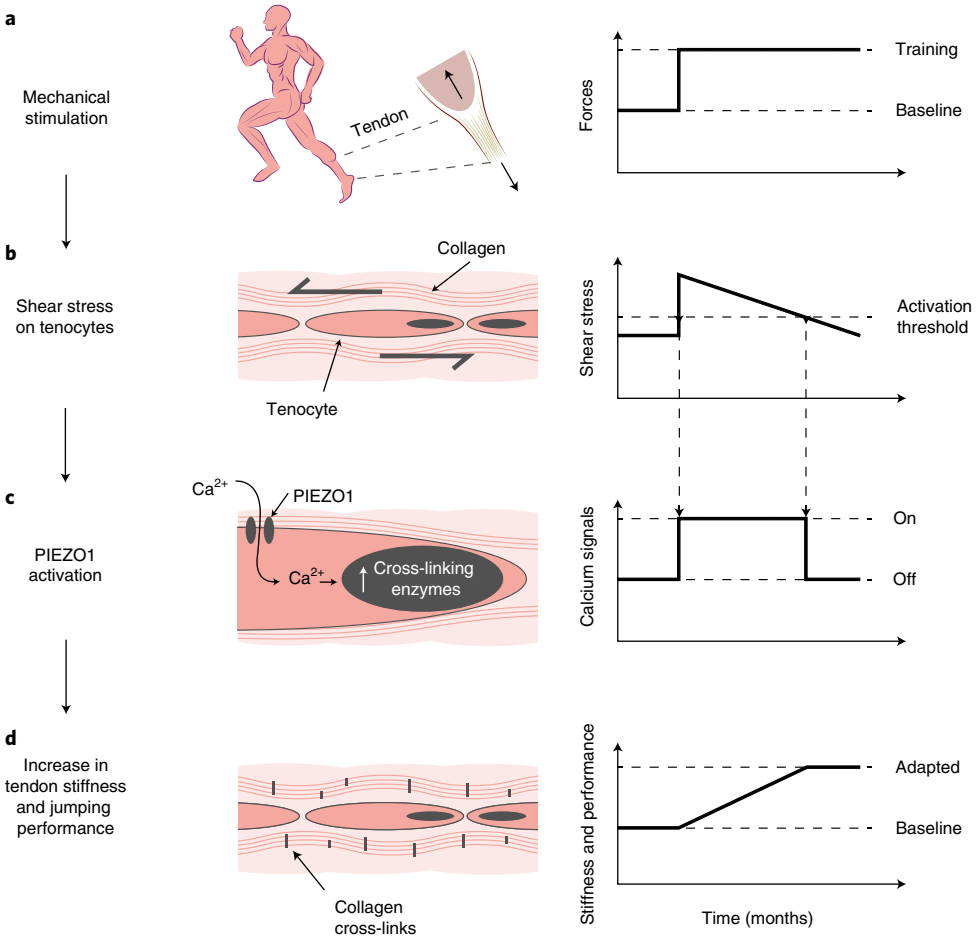

Fig. 8 | Proposed mechanism of tendon mechanotransduction that adapts the tissue and influences physical performance. a,**b**, Mechanical loading of tendons during, for example, training (**a**) causes shear stress on tissue-resident tenocytes (**b**). **c**, Such stimulus is sensed by PIEZO1—a mechanosensitive ion channel—that triggers intracellular Ca^{2+} signals and leads to the upregulation of collagen cross-linking enzymes. **d**, As a consequence, the stiffness of tendons increases, affecting the physical performance.

of type-I collagen. Thus, our data indicate that PIEZO1 regulates the tissue stiffness by adjusting the collagen cross-linking. This mechanism probably modulates the relative motions of collagen fibres and thereby adjusts the shear stress on cells according to the shear sensor—PIEZO1—signalling. Such tendon tissue adaptations presumably imply a tenocyte mechanostat behaviour[60], that is, a feedback mechanism that aims to maintain optimal shear-stress stimuli (Fig. 8). An adapting cross-link network might also explain why exercise has very little to no effect on tissue- and fibril-morphology[43], and why the collagen matrix has a low turnover[61].

The high prevalence of the *PIEZO1*^{GOF} E756del allele in the African population provides the opportunity to study the function of PIEZO1 in humans[31]. The E756del mutation is particularly common in populations of West Africa, probably due to the potential protection it affords against malarial infection[31]. In addition to this potential role, our evidence suggests that the E756del mutation affects human athletic performance. Specifically, E756del carriers perform significantly better than non-carriers in jumping manoeuvres that include high degrees of tendon loading and of energy storage and return[2,52,53]. This performance mechanism is presumably enhanced in tendons of which biomechanical characteristics are governed by an overactive PIEZO1, as we observed an increase in energy return in E756del carriers. Although jumping performance is enabled by the muscle–tendon unit, note that skeletal muscle is probably not affected by the E756del mutation due to the very limited *Piezo1* expression in muscle tissue[16] (Supplementary Fig. 6f). The performance difference in humans as well as the tendon phenotype in mice both emerged at high degrees of tendon loading. Concurrently, both *Piezo1*^{GOF} mice and E756del carriers displayed tendon morphology that is indistinguishable from the wild-type controls. These findings strongly suggest that E756del carriers present a tendon phenotype that is similar to the one observed in *Piezo1*^{GOF} mice.

It is unclear whether the E756del allele is overrepresented in elite sprinters. Yet it will be worth investigating whether the tendon-performance phenotype by E756del carriers is a contributor to the fact that nearly all of the top 500 sprint times of the men's 100 m are held by athletes hailing from countries with high E756del prevalence[49,50].

Beyond implications for athletic performance, PIEZO1 may represent a therapeutic target in clinical indications for which physical rehabilitation is currently prescribed. Tendon pathologies are a common human medical condition, due to the high mechanical demands and the low intrinsic healing capacity of tendon tissues[1,8]. They account for a substantial portion of musculoskeletal diseases, which represent the second leading cause for years lived with disability worldwide[8,62,63]. Our data suggest that pharmacological activation of PIEZO1 stimulates tissue reinforcement mechanisms that may be relevant to treatment of diseased and/or mechanically inferior tendons, perhaps mimicking the effects triggered by

exercise-based physical therapy. Although this is speculative and would require substantial preclinical investigation, the identification of PIEZO1 as a druggable target to drive tissue adaptation could open new paths for clinical treatment of tendon disorders.

Methods

Ca^{2+} imaging of ex vivo tendon fascicles during stretching. Tendon fascicles were gently extracted from the tail of skeletally mature female Wistar rats (aged 14–18 weeks; approval by the Veterinary Office of the Canton of Zurich, ZH235/16). Rat tail tendon fascicles were stained with 5 µM Fluo-4 AM (Thermo Fisher Scientific, F14217) for 2 h at 29 °C and 3% O_2 in a modified Krebs–Henseleit solution (KHS) containing 126 mM NaCl, 3 mM KCl, 2 mM $CaCl_2$, 2 mM $MgSO_4$, 1.25 mM NaH_2PO_4, 26 mM $NaHCO_3$ and 10 mM glucose. Single tendon fascicles were subsequently mounted onto a custom-designed tensile stretching device (equipped with two linear motors and a 20 N load cell) that was placed onto the stage of an iMic widefield microscope (Thermo Fisher Scientific)[64]. During the stretching protocols, fascicles were continually perfused with KHS that was preheated to 29 °C and steadily aerated with a gas mixture containing 95% N_2 and 5% CO_2 to maintain 3% O_2 and constant pH levels. Images were acquired using a ×10/0.4 NA objective with excitation set at 488 nm wavelength and 100 ms exposure time. Before the stretching protocols, fascicles were preconditioned five times to 1.0% initial length L_0 (10 mm mounting length from clamp to clamp). The cross-sectional area was determined using the diameter (assuming a round cross-section) at crimp disappearance and L_0 was defined at 1 MPa tissue stress. Tissue strain was defined as $(L-L_0)/L_0$ as a percentage, with sample length L. Tissue stress was calculated by dividing the force values through the cross-sectional area.

To investigate the cellular response to tissue stretching, single fascicles were stretched at three different strain rates (low, 0.01% strain per s; medium, 0.1% strain per s; high, 1.0% strain per s) from 0% to 10% strain. Baseline activity was investigated at the preload of 1 MPa before initiating the stretching protocol. At medium and high strain rate, time lapses of one z plane were recorded. At low strain rate, a series of image stacks (50 × 2 µm) were acquired and subsequently deconvolved using Huygens Professional v.18.10 (Scientific Volume Imaging) to quantify the micromechanical environment (at the cellular/collagen fibre level) needed to trigger intracellular Ca^{2+} signals. To examine the time lag between the mechanical stimulus and the downstream Ca^{2+} signals, tendon fascicles were subjected to one cycle of 2.7% strain at 30% strain per s.

Time-lapse images were analysed using the following steps. Cell movements were tracked with Imaris v.7.7 (Bitplane) and the exported displacements were further processed using custom software (MATLAB R2016a) that divided the images into 6 × 6 subimages and applied motion correction in each subimage. Ca^{2+} events were automatically detected and measured in the stabilized subimages using CHIPS (Cellular and Hemodynamic Image Processing Suite)[65]. Fibre sliding was calculated from the relative displacements (in the axial direction) of the cells on adjacent fibres (for example, fibre u and v): $\left|\sum_{i=1}^{n} u_{x_i} - \sum_{i=1}^{m} v_{x_i}\right| / L_0$, n and m are the respective cell numbers of the adjacent fibres and L_0 is the fibre length[66].

The Ca^{2+} response of tail tendon fascicles from *Scx-creERT2*; *Piezo1*$^{fl/fl}$ mice and littermate controls (*Piezo1*$^{fl/fl}$ mice) was investigated after staining for 2 h with 5 µM Fluo-4 AM and NucBlue (Thermo Fisher Scientific, R37605). Images were taken using a ×10/0.4 NA objective and excitations of 390 nm (cell nuclei) and 488 nm (Ca^{2+} signal) during the following protocol: fascicles were preloaded to 0.025 N (0% strain), subsequently stretched from 0% to 2% strain at 1% strain per s and then kept at 2% strain. The Ca^{2+} responses of individual cells were analysed using the TrackMate imageJ plugin[67]. Individual cell nuclei were identified and tracked in the images acquired at 390 nm and the cellular Ca^{2+} responses were calculated by averaging the fluorescence signal within a 5 µm radius surrounding the centroids of individual nuclei in the corresponding images acquired at 488 nm. Further analyses were performed using a custom R script. Cells that showed an increase in Ca^{2+} $\Delta F/F > 1.5$ within 30 s from the start of the stretching were categorized as active.

FLIM in tendon fascicles. Isolated rat tail tendon fascicles were stained with 20 µM cell-permeable OGB-1 (Thermo Fisher Scientific, O6806) for 2 h in KHS at 29 °C and 3% O_2 and mounted on our tensile stretching device placed on the stage of a two-photon microscope and continually perfused with KHS during imaging. FLIM was performed on an upright Leica TCS SP8 FLIM two-photon microscope equipped with a tuneable (680–1,300 nm) 80 MHz infrared laser (Insight DS+ Dual, Spectra Physics) and four non-descanned FLIM-enabled hybrid detectors. On the non-descanned detectors, the following emission band-pass filters were used: 460/50 nm, 525/50 nm, 585/40 nm and 650/50 nm. Data acquired from the channels 525/50 nm and 585/40 nm were used for the FLIM analysis. A 2.6 mm working distance Leica HC IRAPO ×25/1.0 NA water-immersion objective was used for imaging. Time-correlated single-photon counting (TCSPC) was performed using a six-channel Picoquant HydraHarp 400 together with the Picoquant Symphotime 64 software package. Femtosecond infrared laser pulses enabled efficient two-photon fluorescence excitation and emission from a thin focal plane in the core of a tendon fascicle (around 30–100 µm deep in the tissue). A laser wavelength of 915 nm and a maximum laser power of 12.5 mW measured after the objective were used to avoid any signs of phototoxicity. To avoid photo-induced effects as well as statistical pile-up effects in the TCSPC histograms, the photon-count rates on the detectors were always kept below 1% of the excitation rate. For fast sequential imaging, an image size of 512 px in width and 80–110 px in height was used with a scanner frequency of 400 Hz.

The Ca^{2+} calibration buffer kit from Thermo Fisher Scientific (C3008MP) was used in combination with the cell-impermeable Ca^{2+} indicator OGB-1 at 1 µM to calibrate the $[Ca^{2+}]$ readout (Supplementary Fig. 2a). Temperature and pH were measured and considered by finely adjusting the estimated $[Ca^{2+}]$ using C. Patton's WEBMAXC program (http://web.stanford.edu/~cpatton/webmaxcS.htm)[34]. The TCSPC histograms were fitted using a double-exponential tailfit within a time gate of 10 ns using the Picoquant Symphotime software. From the tailfit, we calculated the amplitude-weighted average lifetime, which was used throughout the study as a readout for $[Ca^{2+}]$ using a suitable calibration function acquired from fitting a nonlinear Hill function to the OGB-1 calibration data (Supplementary Fig. 2b).

To investigate baseline $[Ca^{2+}]$ in tenocytes, tendon fascicles were imaged at the preload of 1 MPa after a preconditioning. Average image acquisition times were 120 s. A cellular-compartment-dependent region-of-interest analysis was performed to determine Ca^{2+} concentrations in the cytoplasm and in the nucleus. The detected photons within the selected compartments were aggregated to obtain an overall $[Ca^{2+}]$ estimate for that region. Ca^{2+} concentrations during Ca^{2+} signals were examined with two different approaches. First, time lapses were recorded to analyse the $[Ca^{2+}]$ during spontaneous Ca^{2+} signals. Second, time lapses were acquired before and after stretch to study the increase in $[Ca^{2+}]$ induced by mechanical loading. The stretching protocol consisted of a single cycle to 2.7% strain at 1.0% strain per s, starting and ending at the preload. The time lapses were taken over a period of 15 min. To monitor the Ca^{2+} signals, we maximized the temporal FLIM resolution while keeping an appropriate spatial resolution and the total number of collected photons. We therefore adjusted the acquisition rate to 0.066 Hz, which was sufficient to estimate the $[Ca^{2+}]$ during Ca^{2+} events owing to their average duration of around 28 s. The photons were aggregated within the selected single-cell area. Subsequent data analysis calculated the $[Ca^{2+}]$ during Ca^{2+} events. For illustration purposes, we applied a 2 × 2 px binning and a Gaussian filter ($\sigma = 3$) to the pixel maps of the $[Ca^{2+}]$ landscape. However, data analysis and statistics were performed using the raw data, not the filtered pixel maps.

Mathematical model for shear-stress prediction in tenocytes. To predict the shear stress experienced by tenocytes during tissue stretching, we applied a numerical model that assumes cell heights (h) between 1–10 µm and that assumes that individual tenocytes span the distance between two adjacent collagen fibres[68]. Shear stress in tenocytes is generated by unilateral collagen fibre displacement, which leads to transverse displacement of the cell body. By definition, the shear stress (τ) arises through the application of a force (F) parallel to the cross-section over a certain surface (A) and is equal to the shear modulus (G) of the material multiplied by the shear strain (γ). The shear strain is defined as the transverse displacement (Δx) of the material divided by the initial height of the material (h): $\tau = \frac{F}{A} = G \times \gamma = \frac{G \times \Delta x}{h} = \frac{G \times s \times l_{\mathrm{fibre}}}{h}$. The shear modulus of a eukaryotic cell was previously[69] estimated to be around $G = 1.5$ Pa and the transverse material displacement (Δx) was calculated from the fibre sliding (s) and the fibre length ($l_{\mathrm{fibre}} = 900$ µm, corresponding to the width of the field of view). This enables the estimation of shear stresses acting on tenocytes resulting from unilateral collagen fibre sliding.

Primary human and rat tenocyte cultures. Tendon cells were isolated either from fragments of human tendons (flexor digitorum, gracilis and semitendinosus) collected from female and male patients (between 24 and 58 years of age) undergoing treatment at the University Hospital Balgrist (permission 2015–0089 from the institutional review board of the Canton of Zurich and patient-informed consent) or from tail tendon fascicles of skeletally mature female Wistar rats (aged 14–18 weeks; approval by the Veterinary Office of the Canton of Zurich, ZH235/16). Next, tendon tissues were digested with 2 mg ml^{-1} collagenase D (Roche, 11088866001) in Dulbecco's modified Eagle's medium (DMEM/F12, D8437) supplemented with 1% amphotericin B (Gibco, 15290–018) and 1% penicillin–streptomycin (Sigma-Aldrich, P0781) for around 6 h at 37 °C in a humidified atmosphere of 5% CO_2. Isolated cells were cultured on tissue culture plastic in DMEM/F12 with 10% heat-inactivated fetal bovine serum (Gibco, 10500) for 1–2 weeks and subsequently cryopreserved in liquid nitrogen until the start of the experiments.

Ca^{2+} imaging during application of shear stress on isolated tenocytes using flow chambers. Custom-made flow chambers were fabricated using the following procedure. A microscope slide was plasma-treated, and 3 µl of polydimethylsiloxane (PDMS, Sylgard 184 Silicone Elastomer Kit, Dow Europe) was deposited in its centre. A silanized PDMS stamp that was moulded from the negative of the microgroove pattern (10 µm depth/ridge width/pitch) was then placed on top. The assembly was subsequently cured at 70 °C for 6 h before detaching the stamps. PDMS microgrooves were chemically activated using two consecutive treatments of 0.1 mM *N*-sulfosuccinimidyl-6-(4′-azido-2′-nitrophenylamino) hexanoate (CovaChem, 13414) in 50 mM 4-(2-hydroxyethyl)-1-piperazineethanesulfonic acid (Seraglob, K 2101) under

ultraviolet light for 10 min each. Substrates were then washed three times with sterile phosphate-buffered saline (PBS) and coated with 50 µg ml^{-1} collagen-I (Corning, 354249) in PBS overnight at 4 °C, before being washed three times with deionized water and air dried[70]. Finally, a block of PDMS containing a canal (height, 0.4 mm; width, 5 mm; length, 30 mm) was glued on top of the microscope slide, centring the microgrooved patch in the middle of the canal. A fine layer of PDMS containing additional 0.1% platinum-divinyltetramethyldisiloxane (abcr, 146697) was used as glue and cured at 45 °C for 2 h.

Tenocytes were seeded in the flow chamber at a density of 38,000 cells per cm^2 and incubated at 29 °C under 5% CO_2 and 3% O_2 overnight. Staining for 2 h with 1 µM Fluo 4-AM diluted in KHS containing 0.02% pluronic F-127 was performed before placing the flow chamber onto the microscope stage and connecting it to a syringe pump (Cetoni, low-pressure module). Next, the flow chambers were flushed for a few minutes at a flow rate of 0.1 ml min^{-1} (resulting in negligible shear stress of around 0.01 Pa) with KHC that was preheated to 29 °C and degassed to 3% O_2 using a gas mixer. Appropriate flow rates resulting in specific shear stresses on the cell substrate were calculated using established formulas of fluid flow in rectangular channels[71]. During shear-stress experiments, image stacks (5 × 3 µm) were acquired using the iMic widefield microscope (×10 objective) at a frequency of 1 Hz, a wavelength of 488 nm and an exposure time of 100 ms.

Image analysis was performed using an initial average intensity z projection of the image stacks, followed by a segmentation of individual cell bodies performed with a custom ImageJ script based on the fluorescence at the baseline, that is, a 30 s interval before application of the shear-stress stimulus (Supplementary Fig. 3). The mean fluorescence intensity of each segmented cell was normalized to the average intensity measured at the baseline. A Ca^{2+} signal in a cell was defined as such when the normalized fluorescence intensity ($\Delta F/F$) exceeded the baseline fluorescence intensity by 10× the s.d. of the baseline during a 20 s interval after exposure to shear stress.

Generation of CRISPR–Cas9-mediated knockdown cells. Single-guide RNAs (sgRNAs) against multiple candidate genes were designed using the CRISPRdirect online tool (http://crispr.dbcls.jp)[72]. Only highly specific target sites were selected; a list of the respective sequences is provided in Supplementary Table 1. A non-targeting control sgRNA was selected[73] and checked for low targeting potential using a BLASTN 2.8.0 search. Target sequences oligos were synthesized with BsmBI restriction site overhangs by Microsynth and then annealed and cloned into the lentiCRISPRv2 transfer plasmid, a gift from F. Zhang (Addgene plasmid, 52961)[74], according to the protocol provided by the Feng Zhang Lab.

Lentiviral particles were produced by cotransfection of the lentiCRISPRv2 plasmid, containing the respective gRNA-sequence, with the packaging plasmids pCMV-VSV-G (a gift from B. Weinberg; Addgene plasmid, 8454)[75] and psPAX2 (a gift from D. Trono; Addgene plasmid, 12260) into HEK293T cells using Lipofectamine 3000 (Thermo Fisher Scientific, L3000008), according to the manufacturer's instructions.

For transduction, human and rat tenocytes were incubated for 24 h with supernatant containing the viral particles and supplemented with 8 µg ml^{-1} polybrene. Subsequently, human and rat cells were selected with 3 µg ml^{-1} puromycin (Gibco, A1113803) for 3 d or with 4 µg ml^{-1} for 7 d, respectively. The efficiency of the knockouts was tested with quantitative PCR with reverse transcription (RT–qPCR), immunofluorescence and western blotting.

RNA isolation from tissues and cells and RT–qPCR. Freshly isolated tissues were snap-frozen in liquid nitrogen and subsequently homogenized with QIAzol lysis reagent (Qiagen, 79306) using a cryogenic grinder (SPEXSamplePrep FreezerMill 6870). 1-bromo-3-chloropropane (Sigma-Aldrich, B9673) was added to the tissue lysates at a 1:4 ratio, and the RNA-containing aqueous phase was obtained using Phase Lock Gel—Heavy (LabForce, 2302830). In vitro tenocytes were lysed with RLT/bME buffer. Subsequently, RNA from tissue and cell lysates was extracted using the RNeasy micro Kit (Qiagen, 74004) according to the protocol provided by the manufacturer. The quality and quantity of the RNA was measured using a NanoDrop 1000 spectrophotometer (Thermo Fisher Scientific).

RNA was transcribed to cDNA using the High-Capacity cDNA Reverse Transcription Kit with RNase Inhibitor according to the manufacturer instructions (Applied Biosystems, 4374966). Gene expression analysis was performed by RT–qPCR with cDNA corresponding to 10 ng of starting RNA using the PowerUp SYBR Green Master Mix (Thermo Fisher Scientific, A25742) or the KAPA probe fast qPCR Master Mix (2×, KAPA Biosystems, KK4707). The samples were amplified using a StepOnePlus Real-Time PCR System (Applied Biosystems) with the following conditions: 10 min at 95 °C followed by 40 PCR cycles at 95 °C for 15 s and at 60 °C for 1 min. Relative gene expression levels were quantified using the $2^{-\Delta\Delta C_t}$ method, using either *Anxa5* or *Gapdh* as the reference gene. A list of the human and rat primers used with the PowerUp SYBR Green Master Mix is provided in Supplementary Table 2. The rat primers (Thermo Fisher Scientific) used with the KAPA probe fast qPCR Master Mix were as follows: *Anxa5* (Rn00565571_m1), *Lox* (Rn01491829_m1), *Plod2* (Rn00598533_m1) and *Col1a1* (Rn01463848_m1). The mouse primers (Thermo Fisher Scientific) were as follows: *Anxa5* (Mm01293059_m1) and *Piezo1* (Mm01241549_m1).

Immunofluorescence. Cells seeded in flow chambers were fixed with 4% formaldehyde in PBS (Carl Roth, 3105.2) for 20 min at room temperature and subsequently permeabilized with 0.1% Triton X-100 (Axonlab, 10029070) and 0.5% bovine albumin serum (BSA, VWR P6154) in PBS for 10 min. Samples were incubated with specific primary antibodies in PBS with 3% BSA for 1 h and afterwards with a secondary fluorescently labelled antibody. Between every step, samples were washed three times with PBS. Primary antibodies were used against PIEZO1 (Novus Biologicals NBP1–78446 (for human cells), 1:25; Alomone Labs APC-087 (for rat cells), 1:300). Actin filaments were stained with Alexa Fluor 568 phalloidin (Thermo Fisher Scientific, A12380, 1:200) and cell nuclei with NucBlue (Thermo Fisher Scientific, R37605). Alexa-Fluor-488-conjugated donkey anti-rabbit (Thermo Fisher Scientific, A-21206, 1:100) was used as a secondary antibody. Immunofluorescence images were acquired using the iMic spinning-disk confocal microscope using a ×60/1.35 NA oil-immersion objective.

Western blot analysis. Cells were washed with PBS and lysed directly in the cell culture dish with 80 µl of 1× reduced Laemmli buffer (Thermo Fisher Scientific, 15493939) and boiled for 5 min at 95 °C. Next, 15 µl of each sample was loaded onto a 4–15% Mini-PROTEAN TGX stain-free protein gel (Bio-Rad, 4568086). Total protein was analysed using the Criterion Stain-free imaging system (Bio-Rad) and subsequently transferred onto polyvinylidene difluoride membranes using the Trans-Blot-Turbo Transfer System (Bio-Rad). Membrane blocking was performed with 5% non-fat dry milk/TBS-T for 1 h at room temperature. The primary antibodies targeting PIEZO1 (Thermo Fisher Scientific, MA5-32876, 1:500) and β-tubulin (MERCK Millipore, MAB3408, 1:10,000) were diluted in 5% BSA/TBS-T and incubated overnight at 4 °C. Next, the membranes were washed three times in TBS-T and incubated with the secondary antibody (anti-mouse, Sigma-Aldrich, SAB3701073, 1:20,000) for 1 h at room temperature. Images were taken using UltraScence Pico Ultra Western Substrate (GeneDireX, CCH345-B) and the ChemiDoc MP imaging system (Bio-Rad).

Tenocyte-targeted *Piezo1*-knockout mouse. *Scx-creERT2*; *Piezo1*$^{fl/fl}$ mice were generated by crossing *Scx-creERT2* mice (provided A. Huang, Icahn School of Medicine at Mount Sinai) with *Piezo1*$^{fl/fl}$ mice (*Piezo1*$^{tm2.1Aput}$/J; Jackson Laboratory, 029213) to create tamoxifen-inducible tendon-targeted *Piezo1*-knockout mice. For the experiments (approved by the Veterinary Office of the Canton of Zurich, ZH104/2018), male *Scx-creERT2*; *Piezo1*$^{fl/fl}$ mice were mated with female *Piezo1*$^{fl/fl}$ mice. Tamoxifen (Sigma-Aldrich, T5648) in corn oil was given to pups by intragastric injections at P1 (0.05 mg tamoxifen), P2 (0.05 mg) and P3 (0.1 mg). Wild-type littermates (lacking Cre) were used as controls. For gene expression analysis (verification of knockout levels) and Ca^{2+}-imaging experiments, fascicles were isolated from the tails shortly after euthanizing the mice. For biomechanical testing of fascicles, tails were stored at −20 °C after euthanizing the mice.

Tendon explants cultured in bioreactor and subjected to recurrent sham or Yoda1 stimulation. Rat tail tendon fascicles were freshly isolated from female Wistar rats (aged 14–18 weeks) and placed into culture medium (high-glucose Dulbecco's modified Eagle's medium (Sigma-Aldrich, D6429, supplemented with 1% penicillin–streptomycin), 200 µM ascorbic acid (Wako Chemicals 013–19641) and 1% N-2 supplement (Thermo Fisher Scientific, 7001585)). Each fascicle was cut in half, one half was used for mechanical testing at day 0, while the other half was cultured in our custom-made bioreactor[42] at the preload (crimp disappearance, that is, minimal mechanical load) and mechanically tested at day 16. Distal and proximal samples were randomly distributed between the 2 d. Diameters were measured at day 0 and day 16 using a ×10 objective (Motic, AE2000). Cultured fascicles underwent either sham or 5 µM Yoda1 (Sigma-Aldrich SML1558-5MG) stimulations for 30 min on days 0, 3, 6, 9 and 12 after isolation. After the 30 min treatment, fascicles were washed once with medium, then resuspended in medium and incubated at 29 °C under 5% CO_2 and 3% O_2. Ramp-to-failure experiments were performed to assess the biomechanical properties. Samples were preloaded to 0.04 N and preconditioned 5 times to 1% strain. Subsequently, a ramp-to-failure was performed at 1% strain per s. Fascicle stiffness was calculated in the linear region of the force–strain curves and fascicle strength was determined from the maximal force.

Gene expression analysis of fascicles stimulated mechanically or pharmacologically. Rat tail tendon fascicles were freshly extracted from female Wistar rats (aged 14–18 weeks) and placed in the culture medium described above. For the experiment with pharmacological stimulation, fascicles were cultured free-floating and were stimulated with a sham control or a 5 µM Yoda1 (Sigma-Aldrich, SML1558-5MG) for a period of 30 min. For the experiment with mechanical stimulation, fascicles were clamped in our custom bioreactors and either subjected to four-time 2% stretch at 1% per s with a pause of 4 min between each stretch during which fascicles were kept unloaded (stimulated group) or left clamped unloaded (control group). Subsequently, all fascicles were incubated for 48 h at 29 °C under 5% CO_2 and 3% O_2 and then snap-frozen in liquid nitrogen and stored at −80 °C. Sample homogenization, RNA extraction and qPCR were performed as described above.

Biomechanical testing and analysis. The biomechanical properties of tail tendon fascicles and plantaris tendons from female and male *Piezo1*^{GOF} mice[31], *Piezo1*^{cKO} mice and the corresponding wild-type littermates were investigated with ramp-to-failure experiments. Mice were euthanized and stored at either −20 °C or −80 °C until the day of the experiment (approval by the Institutional Animal Care and Use Committees of Scripps Research in accordance with the guidelines established by the Association for Assessment and Accreditation of Laboratory Animal Care International, and approval by the Veterinary Office of the Canton of Zurich, ZH104/2018). After thawing, tail tendon fascicles (from 20–39-week-old *Piezo1*^{GOF} mice, and from 10–13-week-old *Piezo1*^{cKO} mice) and plantaris tendons (from 20–21-week-old *Piezo1*^{GOF} mice) were carefully isolated and tested in uniaxial tension using a custom clamping technique on a universal testing machine that recorded force–displacement data (Zwick Z010 TN, 20 N load-cell). During testing, tendons were kept in a chamber filled with KHS, preloaded to 0.025 N (tail tendon fascicles) or to 0.1 N (plantaris tendons) that corresponds to the initial length L_0 (that is, 0% strain) and preconditioned five times to 1% strain (preload reapplied after every cycle). Subsequently, samples were ramped to failure at a constant strain rate of 1% strain per s. The diameter was measured on the basis of microscopic images of the tail tendon fascicles (×20 objective, Motic, AE2000) and the plantaris tendons (×4 objective), which were taken before the mechanical testing. Tendon stiffness was calculated in the linear region of the force–strain curves and tendon strength was determined from the maximal force.

Two-photon microscopy for assessing cross-link-associated fluorescence. Achilles tendons were isolated from mice (aged 19–39 weeks) that were euthanized and stored at −80 °C. Samples were mounted between a microscopy slide and a cover slide with a drop of PBS. Images were acquired with an upright Leica TCS SP8 MP DIVE FALCON two-photon microscope, equipped with a tunable (680–1,300 nm) 80 MHz laser and four spectrally tunable non-descanned photon-counting hybrid detectors. A ×63/1.2 NA water-immersion objective was used. Autofluorescence signals associated with the collagen cross-links pyridinoline and deoxy-pyridinoline were analysed with 720 nm excitation and 380–425 nm emission[46]; second-harmonic-generation signal associated with the collagen content was investigated with 880 nm excitation and 430–450 nm emission[46]. Laser power ranged from 25 mW to 35 mW. *z* stacks were acquired starting from the tendon surface with 5 planes at 4 µm increments. For each sample, *z* stacks were acquired at four different locations. Image analysis was performed by averaging the intensity signal over the fives planes and the four locations and by calculating the ratio between the averaged cross-links-associated signal and the averaged SHG signal.

Differential scanning calorimetry measurements. Achilles tendons were thawed and placed in PBS for 10 min. After light blotting the sample (that is, a single Achilles tendon) on a paper towel to remove excessive PBS, it was placed in a stainless-steel pan that was sealed with a press[66]. The heat flow was recorded with a differential scanning calorimeter (DSC 2920, TA Instruments) during the following protocol: constant heating rate of 5 °C min^{-1} from 25 °C to 45 °C, followed by a heating rate of 2 °C min^{-1} from 45 °C to 70 °C. An empty pan was used as a reference. The denaturation temperature was determined as the temperature at the peak heat flow. The area of the denaturation curve was calculated by subtracting the heat flow baseline from the heat flow curve (Fig. 6d).

Transmission electron microscopy imaging. Plantaris tendons were freshly isolated from littermates (aged 29–34 weeks) that were euthanized in the middle of the day (normal light–dark cycle) and sequentially fixed with 2.5% glutaraldehyde (Sigma-Aldrich, G5882) in 0.1 M sodium cacodylate buffer (pH 7.2), with 1% OsO_4 in 0.1 M sodium cacodylate buffer at room temperature and with 1% uranyl acetate in H_2O at room temperature for at least 1 h per step. Samples were rinsed three times between the fixation steps and finally with H_2O before dehydration in an ethanol series and embedding in Epon. Ultrathin (70 nm) sections were post-stained with Reynolds lead citrate and imaged in a FEI Talos 120 at 120 kV using a bottom-mounted Ceta camera (CMOS, 4,000 px × 4,000 px) using MAPS software (Thermo Fisher Scientific). Segmentation of the cross-sectional area of collagen fibrils was performed using the Trainable Weka Segmentation Fiji plugin[76].

Activity level and sports participation of the human participants. Healthy self-reported African-American participants (at least 18 years old) were enrolled after approval by the Institutional Review Board of the University of Delaware and written informed consent. A clinical evaluation with ultrasound imaging was performed to ensure that the individuals had no underlying pathologies in their Achilles tendons. Furthermore, the Victorian Institute for Sports Assessment—Achilles questionnaire (VISA-A) was applied to confirm that the Achilles tendons were healthy[77]. Participants reported their highest level of sports participation (recreational, secondary school, collegiate or professional) and their history of sports participation. The Physical Activity Scale was used to assess the individual's reported current physical activity level[78].

Ultrasound-based assessment of the human Achilles tendon morphology. B-mode ultrasound imaging (LOGIQ e ultrasound system (GE Healthcare) with wide-band linear array probe (5.0–13.0 MHz)) was used to analyse the Achilles tendon morphology. In brief, the Achilles tendon cross-sectional area was measured at a distance of 2.5 cm from the calcaneal osteotendinous junction (axial direction) in the images acquired parallel and perpendicular to the fibre orientation (each three repetitions), respectively[79]. Achilles tendon length was measured as the distance from the calcaneal osteotendinous junction to the myotendinous junction of the gastrocnemius and soleus muscles using an extended field of view[79]. The software OsiriX MD (Pixmeo) was used to analyse the ultrasound images.

Functional performance tests. To investigate the jump heights, we used the MuscleLab (Ergotest Innovation) light mat measurement system, which creates an infrared light field 4 mm above the floor and records beam interruptions. The height and weight of participants were recorded before the jumping tests. Jump height was calculated by MuscleLab using the participant weight, ground contact time and flight time. Participants performed two different jump tests. In each test, the participants were asked to place their hands behind their back and to jump as high as possible. The first test was a single leg CMJ in which the participants started by standing on the floor on one leg then quickly bent the knee before jumping straight up as high as possible[80]. This was repeated three times with each leg. The second test was a single leg DCMJ, in which participants jumped off of a 20 cm high box and then jumped vertically as high as possible[80]. For each leg, the average height of three trials was used for analysis.

Genotyping of the human *PIEZO1*^{GOF} (E756del) mutation. Saliva samples were collected using Oragene DNA collection kits (OG-500, DNA Genotek). Isolation of genomic DNA was performed according to the manufacturer's instructions using the prepIT-L2P reagent (PT-L2P, DNA Genotek) included in the kit. The region containing the E756 locus was amplified using PCR (forward primer 5′-CAGGCAGGATGCAGTGAGTG-3′ and reverse primer 5′-GGACATGGCACAGCAGACTG-3′)[31]. This amplicon (around 200 bp) was sequenced using both primers to identify non-carriers and E756del carriers.

Statistical analysis. For multiple comparisons, data were analysed using one-way analysis of variance (ANOVA; Tukey or Dunnett test). Intergroup comparisons were performed using two-tailed Student's *t*-tests or two-tailed Mann–Whitney *U*-tests. For mouse and human data, *n* represents the number of animals or participants; at least $n = 4$ was used. Datasets that included the investigation of more than one tendon from the same animal (for example, multiple tendon fascicles from the same tail, or left and right plantaris) or from the same participant (for example, left and right Achilles tendon) were analysed with linear mixed-effects models (lme4 package in R). For mouse data, the mouse ID was defined as random effect and litter as a fixed effect. For human data, the individual ID was defined as a random effect and leg as a fixed effect. The age, height, weight, highest level of sports participation and activity level of the participants were tested as covariates. In the figures, data are mean ± s.e.m. unless indicated otherwise. Analyses were performed using GraphPad Prism v.8.2 and v.9.0 or RStudio v.1.1.383.

Reporting Summary. Further information on research design is available in the Nature Research Reporting Summary linked to this article.

Data availability

The main data supporting the findings of this study are available within the paper and its Supplementary Information. The raw and analysed datasets generated during the study are too large to be publicly shared, yet they are available from the corresponding author on reasonable request.

Code availability

The software of the stretching device, as well as MATLAB, ImageJ and R codes, are all available from the corresponding author on request. The toolbox CHIPS is freely available[65].

Received: 16 July 2020; Accepted: 17 March 2021;

References

1. Magnusson, S. P., Langberg, H. & Kjaer, M. The pathogenesis of tendinopathy: balancing the response to loading. *Nat. Rev. Rheumatol.* **6**, 262–268 (2010).
2. Dickinson, M. H. et al. How animals move: an integrative view. *Science* **288**, 100–106 (2000).
3. Roberts, T. J., Marsh, R. L., Weyand, P. G. & Taylor, C. R. Muscular force in running turkeys: the economy of minimizing work. *Science* **275**, 1113–1115 (1997).
4. Wilson, A. M., Watson, J. C. & Lichtwark, G. A. Biomechanics: a catapult action for rapid limb protraction. *Nature* **421**, 35–36 (2003).

5. Arampatzis, A., Karamanidis, K. & Albracht, K. Adaptational responses of the human Achilles tendon by modulation of the applied cyclic strain magnitude. *J. Exp. Biol.* **210**, 2743–2753 (2007).
6. Heinemeier, K. M. et al. Uphill running improves rat Achilles tendon tissue mechanical properties and alters gene expression without inducing pathological changes. *J. Appl Physiol.* **113**, 827–836 (2012).
7. Arampatzis, A., Karamanidis, K., Morey-Klapsing, G., De Monte, G. & Stafilidis, S. Mechanical properties of the triceps surae tendon and aponeurosis in relation to intensity of sport activity. *J. Biomech.* **40**, 1946–1952 (2007).
8. Riley, G. Tendinopathy–from basic science to treatment. *Nat. Clin. Pract. Rheumatol.* **4**, 82–89 (2008).
9. Nourissat, G., Berenbaum, F. & Duprez, D. Tendon injury: from biology to tendon repair. *Nat. Rev. Rheumatol.* **11**, 223–233 (2015).
10. Pan, B. et al. TMC1 forms the pore of mechanosensory transduction channels in vertebrate inner ear hair cells. *Neuron* **99**, 736–753 e736 (2018).
11. Ranade, S. S. et al. Piezo2 is the major transducer of mechanical forces for touch sensation in mice. *Nature* **516**, 121–125 (2014).
12. Li, J. et al. Piezo1 integration of vascular architecture with physiological force. *Nature* **515**, 279–282 (2014).
13. Wang, S. et al. Endothelial cation channel PIEZO1 controls blood pressure by mediating flow-induced ATP release. *J. Clin. Invest.* **126**, 4527–4536 (2016).
14. Woo, S. H. et al. Piezo2 is the principal mechanotransduction channel for proprioception. *Nat. Neurosci.* **18**, 1756–1762 (2015).
15. Nonomura, K. et al. Piezo2 senses airway stretch and mediates lung inflation-induced apnoea. *Nature* **541**, 176–181 (2017).
16. Coste, B. et al. Piezo1 and Piezo2 are essential components of distinct mechanically activated cation channels. *Science* **330**, 55–60 (2010).
17. Kang, L., Gao, J., Schafer, W. R., Xie, Z. & Xu, X. S. *C. elegans* TRP family protein TRP-4 is a pore-forming subunit of a native mechanotransduction channel. *Neuron* **67**, 381–391 (2010).
18. Servin-Vences, M. R., Moroni, M., Lewin, G. R. & Poole, K. Direct measurement of TRPV4 and PIEZO1 activity reveals multiple mechanotransduction pathways in chondrocytes. *eLife* **6**, e21074 (2017).
19. Patel, A. J. et al. A mammalian two pore domain mechano-gated S-like K^+ channel. *EMBO J.* **17**, 4283–4290 (1998).
20. Maingret, F., Fosset, M., Lesage, F., Lazdunski, M. & Honoré, E. TRAAK is a mammalian neuronal mechano-gated K^+ channel. *J. Biol. Chem.* **274**, 1381–1387 (1999).
21. Xu, J. et al. GPR68 senses flow and is essential for vascular physiology. *Cell* **173**, 762–775 e716 (2018).
22. O'Hagan, R., Chalfie, M. & Goodman, M. B. The MEC-4 DEG/ENaC channel of *Caenorhabditis elegans* touch receptor neurons transduces mechanical signals. *Nat. Neurosci.* **8**, 43–50 (2005).
23. Zhang, M. et al. Structure of the mechanosensitive OSCA channels. *Nat. Struct. Mol. Biol.* **25**, 850–858 (2018).
24. Murthy, S. E. et al. OSCA/TMEM63 are an evolutionarily conserved family of mechanically activated ion channels. *eLife* **7**, e41844 (2018).
25. Lukacs, V. et al. Impaired PIEZO1 function in patients with a novel autosomal recessive congenital lymphatic dysplasia. *Nat. Commun.* **6**, 8329 (2015).
26. Fotiou, E. et al. Novel mutations in PIEZO1 cause an autosomal recessive generalized lymphatic dysplasia with non-immune hydrops fetalis. *Nat. Commun.* **6**, 8085 (2015).
27. Retailleau, K. et al. Piezo1 in smooth muscle cells is involved in hypertension-dependent arterial remodeling. *Cell Rep.* **13**, 1161–1171 (2015).
28. Peyronnet, R. et al. Piezo1-dependent stretch-activated channels are inhibited by polycystin-2 in renal tubular epithelial cells. *EMBO Rep.* **14**, 1143–1148 (2013).
29. Cahalan, S. M. et al. Piezo1 links mechanical forces to red blood cell volume. *eLife* **4**, e07370 (2015).
30. Sun, W. et al. The mechanosensitive Piezo1 channel is required for bone formation. *eLife* **8**, e47454 (2019).
31. Ma, S. et al. Common PIEZO1 allele in African populations causes RBC dehydration and attenuates *Plasmodium* infection. *Cell* **173**, 443–455 (2018).
32. Stauber, T., Blache, U. & Snedeker, J. G. Tendon tissue microdamage and the limits of intrinsic repair. *Matrix Biol.* **85-86**, 68–79 (2020).
33. Snedeker, J. G., Ben Arav, A., Zilberman, Y., Pelled, G. & Gazit, D. Functional fibered confocal microscopy: a promising tool for assessing tendon regeneration. *Tissue Eng. C* **15**, 485–491 (2009).
34. Zheng, K. et al. Time-resolved imaging reveals heterogeneous landscapes of nanomolar Ca^{2+} in neurons and astroglia. *Neuron* **88**, 277–288 (2015).
35. Screen, H. R., Lee, D. A., Bader, D. L. & Shelton, J. C. An investigation into the effects of the hierarchical structure of tendon fascicles on micromechanical properties. *Proc. Inst. Mech. Eng. H* **218**, 109–119 (2004).
36. Murthy, S. E., Dubin, A. E. & Patapoutian, A. Piezos thrive under pressure: mechanically activated ion channels in health and disease. *Nat. Rev. Mol. Cell Biol.* **18**, 771–783 (2017).
37. Wunderli, S. L. et al. Tendon response to matrix unloading is determined by the patho-physiological niche. *Matrix Biol.* **89**, 11–26 (2020).
38. Peffers, M. J. et al. Transcriptome analysis of ageing in uninjured human Achilles tendon. *Arthritis Res. Ther.* **17**, 33 (2015).
39. Ranade, S. S. et al. Piezo1, a mechanically activated ion channel, is required for vascular development in mice. *Proc. Natl Acad. Sci. USA* **111**, 10347–10352 (2014).
40. Howell, K. et al. Novel model of tendon regeneration reveals distinct cell mechanisms underlying regenerative and fibrotic tendon healing. *Sci. Rep.* **7**, 45238 (2017).
41. Syeda, R. et al. Chemical activation of the mechanotransduction channel Piezo1. *eLife* **4**, e07369 (2015).
42. Wunderli, S. L. et al. Minimal mechanical load and tissue culture conditions preserve native cell phenotype and morphology in tendon-a novel ex vivo mouse explant model. *J. Orthop. Res.* **36**, 1383–1390 (2018).
43. Couppé, C. et al. Life-long endurance running is associated with reduced glycation and mechanical stress in connective tissue. *Age* **36**, 9665 (2014).
44. Thorpe, C. T., Stark, R. J., Goodship, A. E. & Birch, H. L. Mechanical properties of the equine superficial digital flexor tendon relate to specific collagen cross-link levels. *Equine Vet. J. Suppl.* **42**, 538–543 (2010).
45. Zeeman, R. et al. Successive epoxy and carbodiimide cross-linking of dermal sheep collagen. *Biomaterials* **20**, 921–931 (1999).
46. Marturano, J. E., Xylas, J. F., Sridharan, G. V., Georgakoudi, I. & Kuo, C. K. Lysyl oxidase-mediated collagen crosslinks may be assessed as markers of functional properties of tendon tissue formation. *Acta Biomater.* **10**, 1370–1379 (2014).
47. Mersha, T. B. & Abebe, T. Self-reported race/ethnicity in the age of genomic research: its potential impact on understanding health disparities. *Hum. Genomics* **9**, 1 (2015).
48. Yancy, C. W. & McNally E. Reporting genetic markers and the social determinants of health in clinical cardiovascular research—it is time to recalibrate the use of race. *JAMA Cardiol.* https://doi.org/10.1001/jamacardio.2020.6576 (2020).
49. Athletics—100m men. *Olympic Games* www.olympic.org/athletics/100m-men (accessed May 2020).
50. 100 meters men. *World Athletics* www.worldathletics.org/records/all-time-toplists/sprints/100-metres/outdoor/men/senior (accessed May 2020).
51. Long jump men. *World Athletics* www.worldathletics.org/records/all-time-toplists/jumps/long-jump/outdoor/men/senior (accessed May 2020).
52. Ishikawa, M., Niemela, E. & Komi, P. V. Interaction between fascicle and tendinous tissues in short-contact stretch-shortening cycle exercise with varying eccentric intensities. *J. Appl Physiol.* **99**, 217–223 (2005).
53. Earp, J. E. et al. Influence of muscle-tendon unit structure on rate of force development during the squat, countermovement, and drop jumps. *J. Strength Cond. Res.* **25**, 340–347 (2011).
54. Lavagnino, M. et al. Tendon mechanobiology: current knowledge and future research opportunities. *J. Orthop. Res.* **33**, 813–822 (2015).
55. Arnoczky, S. P., Lavagnino, M. & Egerbacher, M. The response of tendon cells to changing loads: implications in the etiopathogenesis of tendinopathy. *Tendinopathy Athl.* **1**, 46–59 (2007).
56. Wall, M. E. & Banes, A. J. Early responses to mechanical load in tendon: role for calcium signaling, gap junctions and intercellular communication. *J. Musculoskelet. Neuronal Interact.* **5**, 70–84 (2005).
57. Maeda, E., Hagiwara, Y., Wang, J. H. & Ohashi, T. A new experimental system for simultaneous application of cyclic tensile strain and fluid shear stress to tenocytes in vitro. *Biomed. Microdevices* **15**, 1067–1075 (2013).
58. Kongsgaard, M. et al. Corticosteroid injections, eccentric decline squat training and heavy slow resistance training in patellar tendinopathy. *Scand. J. Med. Sci. Sports* **19**, 790–802 (2009).
59. Beyer, R. et al. Heavy slow resistance versus eccentric training as treatment for achilles tendinopathy: a randomized controlled trial. *Am. J. Sports Med.* **43**, 1704–1711 (2015).
60. Frost, H. M. Bone "mass" and the "mechanostat": a proposal. *Anat. Rec.* **219**, 1–9 (1987).
61. Heinemeier, K. M., Schjerling, P., Heinemeier, J., Magnusson, S. P. & Kjaer, M. Lack of tissue renewal in human adult Achilles tendon is revealed by nuclear bomb ^{14}C. *FASEB J.* **27**, 2074–2079 (2013).
62. Forde, M. S., Punnett, L. & Wegman, D. H. Prevalence of musculoskeletal disorders in union ironworkers. *J. Occup. Environ. Hyg.* **2**, 203–212 (2005).
63. Sebbag, E. et al. The world-wide burden of musculoskeletal diseases: a systematic analysis of the World Health Organization Burden of Diseases Database. *Ann. Rheum. Dis.* **78**, 844–848 (2019).
64. Gautieri, A. et al. Advanced glycation end-products: mechanics of aged collagen from molecule to tissue. *Matrix Biol.* **59**, 95–108 (2017).
65. Barrett, M. J. P., Ferrari, K. D., Stobart, J. L., Holub, M. & Weber, B. CHIPS: an extensible toolbox for cellular and hemodynamic two-photon image analysis. *Neuroinformatics* **16**, 145–147 (2018).
66. Li, Y., Fessel, G., Georgiadis, M. & Snedeker, J. G. Advanced glycation end-products diminish tendon collagen fiber sliding. *Matrix Biol.* **32**, 169–177 (2013).

67. Tinevez, J.-Y. et al. TrackMate: an open and extensible platform for single-particle tracking. *Methods* **115**, 80–90 (2017).
68. McNeilly, C. M., Banes, A. J., Benjamin, M. & Ralphs, J. R. Tendon cells in vivo form a three dimensional network of cell processes linked by gap junctions. *J. Anat.* **189**, 593–600 (1996).
69. Song, M. J. et al. Mapping the mechanome of live stem cells using a novel method to measure local strain fields in situ at the fluid-cell interface. *PLoS ONE* **7**, e43601 (2012).
70. Razafiarison, T., Silvan, U., Meier, D. & Snedeker, J. G. Surface-driven collagen self-assembly affects early osteogenic stem cell signaling. *Adv. Healthc. Mater.* **5**, 1481–1492 (2016).
71. Cornish, R. Flow in a pipe of rectangular cross-section. *Proc. R. Soc. A* **120**, 691–700 (1928).
72. Naito, Y., Hino, K., Bono, H. & Ui-Tei, K. CRISPRdirect: software for designing CRISPR/Cas guide RNA with reduced off-target sites. *Bioinformatics* **31**, 1120–1123 (2015).
73. Morgens, D. W. et al. Genome-scale measurement of off-target activity using Cas9 toxicity in high-throughput screens. *Nat. Commun.* **8**, 15178 (2017).
74. Sanjana, N. E., Shalem, O. & Zhang, F. Improved vectors and genome-wide libraries for CRISPR screening. *Nat. Methods* **11**, 783–784 (2014).
75. Stewart, S. A. et al. Lentivirus-delivered stable gene silencing by RNAi in primary cells. *RNA* **9**, 493–501 (2003).
76. Arganda-Carreras, I. et al. Trainable Weka segmentation: a machine learning tool for microscopy pixel classification. *Bioinformatics* **33**, 2424–2426 (2017).
77. Robinson, J. M. et al. The VISA-A questionnaire: a valid and reliable index of the clinical severity of Achilles tendinopathy. *Br. J. Sports Med.* **35**, 335–341 (2001).
78. Grimby, G. Physical activity and muscle training in the elderly. *Acta Med. Scand. Suppl.* **711**, 233–237 (1986).
79. Silbernagel, K. G., Shelley, K., Powell, S. & Varrecchia, S. Extended field of view ultrasound imaging to evaluate Achilles tendon length and thickness: a reliability and validity study. *Muscles Ligaments Tendons J.* **6**, 104–110 (2016).
80. Silbernagel, K. G., Gustavsson, A., Thomee, R. & Karlsson, J. Evaluation of lower leg function in patients with Achilles tendinopathy. *Knee Surg. Sports Traumatol. Arthrosc.* **14**, 1207–1217 (2006).

Acknowledgements

We thank A. Ziegler for software assistance; N. Wili for support in chemistry; B. Rutishauser and E. Bachmann for engineering assistance; L. Gasser (Statistical Consulting Group, ETH Zurich) for statistical support; members of the Snedeker group for constructive discussions; A. Huang and R. Schweitzer for providing *Scx-creERT2* mice; A. Patapoutian for providing *Piezo1*^{GOF} mice and feedback; U. Lüthi and A. Käch from the Center for Microscopy and Image Analysis (University of Zurich) for help with transmission electron microscopy; R. Mezzenga and Y. Yao (ETH Zurich) for access to the differential scanning calorimeter and assistance during the experiments; and P. Aagaard for insights on the human jumping performance data. Funding was provided by the Swiss National Science Foundation (grant numbers 165670 and 185095).

Author contributions

F.S.P., P.K.J., A.S.S. and J.G.S. designed experiments and wrote the manuscript. F.S.P. performed the Ca^{2+}-imaging experiments with tendon explants. F.S.P., K.D.F., D.H., S.C., A.N.H., U.S. and B.W. designed and analysed the Ca^{2+}-imaging experiments. P.K.J. and F.S.P. carried out and analysed the shear-stress experiments. M.J.A., F.S.P., M.B. and B.P.-T. generated and analysed the knockout cells. S.F.F., M.B. and U.B. helped with human tendon tissues and isolation of primary cells. F.S.P. and S.M. performed mouse experiments. S.H., K.G.S., F.S.P. and J.G.S. designed and performed the human study. F.S.P. and B.P.-T. carried out human genotyping. F.S.P., S.H. and T.G. analysed the human data. All of the authors provided feedback on the manuscript.

Competing interests

The authors declare no competing interests.

Additional information

Supplementary information The online version contains supplementary material available at https://doi.org/10.1038/s41551-021-00716-x.

Correspondence and requests for materials should be addressed to J.G.S.

Peer review information *Nature Biomedical Engineering* thanks Michael Lavagnino and the other, anonymous, reviewer(s) for their contribution to the peer review of this work. Peer reviewer reports are available.

Reprints and permissions information is available at www.nature.com/reprints.

Publisher's note Springer Nature remains neutral with regard to jurisdictional claims in published maps and institutional affiliations.

nature research

Corresponding author(s): Jess G. Snedeker

Last updated by author(s): Mar 12, 2021

Reporting Summary

Nature Research wishes to improve the reproducibility of the work that we publish. This form provides structure for consistency and transparency in reporting. For further information on Nature Research policies, see our Editorial Policies and the Editorial Policy Checklist.

Statistics

For all statistical analyses, confirm that the following items are present in the figure legend, table legend, main text, or Methods section.

n/a	Confirmed	
☐	☒	The exact sample size (*n*) for each experimental group/condition, given as a discrete number and unit of measurement
☐	☒	A statement on whether measurements were taken from distinct samples or whether the same sample was measured repeatedly
☐	☒	The statistical test(s) used AND whether they are one- or two-sided *Only common tests should be described solely by name; describe more complex techniques in the Methods section.*
☐	☒	A description of all covariates tested
☐	☒	A description of any assumptions or corrections, such as tests of normality and adjustment for multiple comparisons
☐	☒	A full description of the statistical parameters including central tendency (e.g. means) or other basic estimates (e.g. regression coefficient) AND variation (e.g. standard deviation) or associated estimates of uncertainty (e.g. confidence intervals)
☐	☒	For null hypothesis testing, the test statistic (e.g. *F*, *t*, *r*) with confidence intervals, effect sizes, degrees of freedom and *P* value noted *Give P values as exact values whenever suitable.*
☒	☐	For Bayesian analysis, information on the choice of priors and Markov chain Monte Carlo settings
☒	☐	For hierarchical and complex designs, identification of the appropriate level for tests and full reporting of outcomes
☒	☐	Estimates of effect sizes (e.g. Cohen's *d*, Pearson's *r*), indicating how they were calculated

Our web collection on statistics for biologists contains articles on many of the points above.

Software and code

Policy information about availability of computer code

Data collection	TILL Photonics Live Acquisition, custom-developed software of stretching device implemented in C++ within the QT framework with integrated third-party libraries, Leica Application Suite X, Picoquant Symphotime 64 FLIM, neMESYS (Cetoni), ChemiDoc MP imaging system (Bio-Rad), MAPS (Thermo Fisher Scientific), testXpert II (ZwickRoell), Motic Images Plus 2.0, GE Logiq e ultrasound (GE Healthcare), and MuscleLab (Ergotest Innovation).
Data analysis	CHIPS (Cellular and Hemodynamic Image Processing Suite), MATLAB R2016a and R2019a, Huygens Professional 18.10 (Scientific Volume Imaging), Imaris 7.7 (Bitplane AG), ImageJ 1.51 and 1.52, Picoquant Symphotime 64 FLIM, RStudio v1.1.383, GraphPad Prism 8.2, OsiriX MD (Pixmeo SARL), and MuscleLab (Ergotest Innovation).

For manuscripts utilizing custom algorithms or software that are central to the research but not yet described in published literature, software must be made available to editors and reviewers. We strongly encourage code deposition in a community repository (e.g. GitHub). See the Nature Research guidelines for submitting code & software for further information.

Data

Policy information about availability of data

All manuscripts must include a data availability statement. This statement should provide the following information, where applicable:

- Accession codes, unique identifiers, or web links for publicly available datasets
- A list of figures that have associated raw data
- A description of any restrictions on data availability

The main data supporting the findings of this study are available within the paper and its Supplementary Information. The raw and analysed datasets generated during the study are too large to be publicly shared, yet they are available from the corresponding authors upon reasonable request.

Field-specific reporting

Please select the one below that is the best fit for your research. If you are not sure, read the appropriate sections before making your selection.

☒ Life sciences ☐ Behavioural & social sciences ☐ Ecological, evolutionary & environmental sciences

For a reference copy of the document with all sections, see nature.com/documents/nr-reporting-summary-flat.pdf

Life sciences study design

All studies must disclose on these points even when the disclosure is negative.

Sample size	The sample sizes were determined on the basis of comparable experiments reported in the literature and on the basis of the consistency and magnitude of the measurable changes. The number of participants of the human study was predetermined with a power analysis.
Data exclusions	In three participants of the human study, we found an additional mutation (E750Q) very close to the E756del mutation on the same chromosome. These three participants were excluded, due to the unknown consequence of the double mutation on the kinetics of the PIEZO1 channel. No other data were excluded.
Replication	We performed multiple independent experiments, as described in the figure legends. The results were reproducible.
Randomization	Knockout cells were assigned to the experimental group according to the specific gene that was modified. Mice and human participants were allocated into the experimental groups according to their genotype. For mice, factors such as animal ID, litter and age were included in the analysis. For humans, the following factors were included in the analysis: participant ID, age, weight, height, levels of activity and sports participation.
Blinding	During experiments with cells and mice, the investigators were not blinded to group allocation, as data analysis was performed automatically with the same scripts for every experimental group. During the human study, investigators as well as participants were blinded to group allocation. Genotyping was performed after data collection.

Reporting for specific materials, systems and methods

We require information from authors about some types of materials, experimental systems and methods used in many studies. Here, indicate whether each material, system or method listed is relevant to your study. If you are not sure if a list item applies to your research, read the appropriate section before selecting a response.

Materials & experimental systems

n/a	Involved in the study
☐	☒ Antibodies
☐	☒ Eukaryotic cell lines
☒	☐ Palaeontology and archaeology
☐	☒ Animals and other organisms
☐	☒ Human research participants
☒	☐ Clinical data
☒	☐ Dual use research of concern

Methods

n/a	Involved in the study
☒	☐ ChIP-seq
☒	☐ Flow cytometry
☒	☐ MRI-based neuroimaging

Antibodies

Antibodies used	Rabbit polyclonal anti-human PIEZO1, Novus Biologicals Cat# NBP1-78446, dilution 1:25 Rabbit polyclonal anti-rat PIEZO1, Alomone Labs Cat# APC-087, dilution 1:300 Alexa Fluor 488 conjugated donkey polyclonal anti-rabbit IgG, Thermo Fisher Scientific Cat# A-21206, dilution 1:100 Mouse monoclonal anti-human PIEZO1, Thermo Fisher Scientific Cat# MA5-32876, dilution 1:500 Mouse monoclonal anti-human Tubulin beta, MERCK Millipore Cat# MAB3408, dilution 1:10'000 Rabbit polyclonal anti-mouse IgG, Sigma-Aldrich Cat# SAB3701073, dilution 1:20'000
Validation	All three anti-PIEZO1 antibodies showed clearly reduced signal in CRISPR-Cas9-mediated Piezo1-knockout cells.

Eukaryotic cell lines

Policy information about cell lines

Cell line source(s)	HEK 293T/17 cells were acquired from the American Type Culture Collection (ATCC).

Authentication	HEK 293T/17 cells were authenticated by American Type Culture Collection (ATCC).
Mycoplasma contamination	HEK 293T/17 cells were not tested for mycoplasma contamination.
Commonly misidentified lines (See ICLAC register)	No commonly misidentified cell lines were used.

Animals and other organisms

Policy information about studies involving animals; ARRIVE guidelines recommended for reporting animal research

Laboratory animals	Rats: Wistar (from Janvier-Labs), females, 14–18 weeks of age, 250–350 g of weight. Mice strains: Piezo1GOF mice, in C57BL/6 background, females and males, 20–39 weeks of age, 25–35 g of weight. Piezo1 knockout mice, in C57BL/6 background, females and males, 7–13 weeks of age, 20–30 g of weight.
Wild animals	The study did not involve wild animals.
Field-collected samples	The study did not involve samples collected from the field.
Ethics oversight	Veterinary Authorities of the Canton of Zurich, Institutional Animal Care and Use Committees of Scripps Research.

Note that full information on the approval of the study protocol must also be provided in the manuscript.

Human research participants

Policy information about studies involving human research participants

Population characteristics	Females and males, 18–36 years old, healthy individuals of African descent (African Americans), 22 carrying the E756del allele and 43 carrying the wild-type allele, all with healthy Achilles tendons.
Recruitment	Recruitment flyers were posted in the community, in the University of Delaware physical therapy clinic, and through local referral sources in the area. Results are likely not biased by the recruitment because of the unknown genotype at the time of recruitment. Saliva samples were processed after data collection.
Ethics oversight	Institutional Review Board of the University of Delaware.

Note that full information on the approval of the study protocol must also be provided in the manuscript.